AN ISOGEOMETRIC CONFORMING KIRCHHOFF PLATE ELEMENT USING RATIONAL BÉZIER BASIS FUNCTIONS

BY

MR. VITHEARIN CHORN

A THESIS SUBMITTED IN PARTIAL FULFILLMENT OF THE REQUIREMENTS FOR THE DEGREE OF MASTER OF SCIENCE (ENGINEERING AND TECHNOLOGY)

SIRINDHORN INTERNATIONAL INSTITUTE OF TECHNOLOGY

THAMMASAT UNIVERSITY

ACADEMIC YEAR 2019

AN ISOGEOMETRIC CONFORMING KIRCHHOFF PLATE ELEMENT USING RATIONAL BÉZIER BASIS FUNCTIONS

BY

MR. VITHEARIN CHORN

A THESIS SUBMITTED IN PARTIAL FULFILLMENT OF THE REQUIREMENTS FOR THE DEGREE OF MASTER OF SCIENCE (ENGINEERING AND TECHNOLOGY)
SIRINDHORN INTERNATIONAL INSTITUTE OF TECHNOLOGY
THAMMASAT UNIVERSITY
ACADEMIC YEAR 2019

THAMMASAT UNIVERSITY
SIRINDHORN INTERNATIONAL INSTITUTE OF TECHNOLOGY

THESIS

BY

MR. VITHEARIN CHORN

ENTITLED

AN ISOGEOMETRIC CONFORMING KIRCHHOFF PLATE ELEMENT USING RATIONAL BÉZIER BASIS FUNCTIONS

was approved as partial fulfillment of the requirements for
the degree of Master of Science (Engineering and Technology)

on May 28, 2019

Chairman Chainarong Athisakul

(Assistant Professor Chainarong Athisakul, Ph.D.)

Member and Advisor

(Professor Pruettha Nanakorn, D.Eng.)

Member

(Ganchai Tanapornraweekit, Ph.D.)

Director

(Professor Pruettha Nanakorn, D.Eng.)

Thesis Title	AN ISOGEOMETRIC CONFORMING KIRCHHOFF PLATE ELEMENT USING RATIONAL BÉZIER BASIS FUNCTIONS
Author	Mr. Vithearin Chorn
Degree	Master of Science (Engineering and Technology)
Faculty/University	Sirindhorn International Institute of Technology/ Thammasat University
Thesis Advisor	Professor Pruettha Nanakorn, D.Eng.
Academic Years	2019

ABSTRACT

A considerable number of research works to develop conforming Kirchhoff plate elements under small displacements have been performed during the last decades. Several types of interpolation function and degrees of freedom are used in such a way that the continuity of displacements and rotational displacements across elements is ensured. Polynomials are undoubtedly the most preferred choices for approximation of unknown displacements and representation of plate geometry. However, they stop being effective when plates with complex geometry are considered. In this study, an isogeometric quadrilateral conforming Kirchhoff plate element is proposed. The geometry of the proposed quadrilateral plate element and the displacement fields are approximated by using rational Bézier basis functions. The starting point of this study is to transform the element unknowns initially written in terms of control variables into the final degrees of freedom that include the displacements and rotations of the corner nodes and the normal rotations of the edge nodes. For this purpose, a transformation between control variables and degrees of freedom is derived. Multiple constraints between degrees of freedom are required for the derivation of the transformation, and they are handled by means of the penalty method. With such approach, this proposed element passes the bending patch test. The proposed element is examined by some benchmark problems having distorted meshes and curved edges. The robustness and the rate of convergence of the element are found to be satisfactory.

Keywords: Conforming element, Kirchhoff plate, Rational Bézier basis functions, Isogeometric, Penalty method, Curved edge, Quadrilateral element, Optimal rate of convergence,

ACKNOWLEDGEMENTS

Being able to complete this thesis, I would like to express my deep appreciation and sincere gratitude to Professor Pruettha Nanakorn, my research advisor for his invaluable suggestions, recommendations, continuous supports and encouragement during my research process. I have learnt various aspects from him, e.g., academic skills that include technical works and disciplines during my master's degree journey.

I would also like to express my sincere gratitude to Mr. Duy Vo, my research senior for his constructive advice and comments. He always provides reasonable explanation and encourages me to stay positive during the difficult times in my research journey.

My deep respectful acknowledgement is extended to my parents, two aunties, and my families for their endless love and continuous supports since I have started my study. Without them, I would not have come this far.

My grateful acknowledgement expressed to Assistant Professor Chainarong Athisakul, the chairman of the thesis committee and to Dr. Ganchai Tanapornraweekit, my thesis committee member for their valuable time participating in my research presentations, invaluable comments, questions, and recommendations for improving the qualities of my thesis.

I would like to express my special thanks to SIIT and Thammasat university (TU) for granting me a SIIT-TU scholarship that supported me during my master's degree life. In addition, my sincere appreciation is extended to the lecturers at SIIT for their invaluable courses, which helped me gain a lot of understanding, and to all the staff members for their academic assistances in terms of my academic document preparation and validation.

My special thanks are also extended to my girlfriend, and my two best friends for their good advice and continuous encouragement.

Mr. Vithearin Chorn

TABLE OF CONTENTS

	Page
ABSTRACT	(1)
ACKNOWLEDGEMENTS	(3)
LIST OF TABLES	(6)
LIST OF FIGURES	(7)
CHAPTER 1 INTRODUCTION	1
1.1 General	1
1.2 Problem statement	2
1.3 The objectives of the study	4
1.4 The scope of the study	4
CHAPTER 2 LITERATURE REVIEW	5
CHAPTER 3 THEORETICAL BACKGROUND	8
3.1 Kirchhoff plate theory	8
3.1.1 Kinematics	8
3.1.2 Strain measurement and stress resultants	9
3.1.3 Virtual work equation for a Kirchhoff plate	10
3.2 Non-conforming 4-noded MZC rectangular plate element	11
3.3 Conforming element 4-noded BFS rectangular element	15
3.4 Bernstein polynomials and rational Bézier surfaces	18
3.4.1 Bézier curves	18
3.4.2 Rational Bézier surfaces	20
CHAPTER 4 THE BI-CUBIC BÉZIER QUADRILATERAL CONFORMING PLATE ELEMENT	24
4.1 Approximations of the geometry and deflection of the plate element	24

4.2 The finite element equation and unique transformation 25
4.3 The constrained finite element formulation 33

CHAPTER 5 NUMERICAL EXAMPLES 35
5.1 Patch test with a constant bending moment 35
5.2 A Simply supported square plate 38
5.3 A clamped circular plate 43
5.4 Clamped cutout square plate 46

CHAPTER 6 CONCLUSIONS 49

REFERENCES 51

BIOGRAPHY 54

LIST OF TABLES

Table	Page
5.1 Simply supported square plate (Mesh 1).	41
5.2 Simply supported square plate (Mesh 2).	42
5.3 Simply supported square plate (Mesh 3).	42
5.4 The numerical results and percentage errors of the central deflection of the circular plate.	45
5.5 Numerical results for cutout square plate.	48

LIST OF FIGURES

Figure Page

3.1 Coordinates system of a plate with conventions of internal and external forces. 9

3.2 Non-conforming 4-noded MZC. 12

3.3 Non-conforming 4-noded MZC (a): displacement, (b): rotation around y axis, and (c): rotation around x axis. 15

3.4 Conforming element 4-noded BFS. 17

3.5 Conforming element 4-noded BFS. (a): displacement, (b): rotation around y axis, and (c): rotation around x axis. 18

3.6 Cubic Bernstein basis functions. 19

3.7 Cubic Bézier curve. 20

3.8 Representation of a circle by quadratic Bézier and quadratic rational Bézier curves. (a): quadratic rational Bézier curves, (b): quadratic Bézier curves 21

3.9 A flat surface with curved boundaries represented by a rational Bézier surface. 23

4.1 Bi-cubic rational Bézier representation of a quarter of an annulus. 25

4.2 The proposed quadrilateral element. (a): Nodal parametric coordinates, (b): Nodal degrees of freedom. 28

4.3 Normal rotations. 32

4.4 The proposed quadrilateral element – Local transformations. (a): Degrees of freedom, (b): Control variables. 32

4.5 The proposed quadrilateral element – Affected control variables and degrees of freedom of element sides. (a): side 1, (b): side 2. 33

5.1 A square simply supported plate with a constant bending moment. (a): Loading and boundary conditions, (b): Mesh definition. 36

5.2 A square simply supported plate with a constant bending moment. (a): Deflections of three meshes, (b): Deformation of the plate. 37

5.3 A square simply supported plate with a constant bending moment – influence of the penalty parameter to the deflection at the center. 37

5.4 A simply supported square plate – Problem set up. 38

5.5 A simply supported square plate – Unstructured meshes. (a): Mesh 1, (b): Mesh 2, (c): Mesh 3. 39

5.6 A simply supported square plate – Deformations with 8×8 elements for $a = L/4$. (a): Mesh 1, (b): Mesh 2, (c): Mesh 3. 39

5.7 A simply supported square plate – Deformations with 8×8 elements for $a = L/4$. (a): Mesh 1, (b): Mesh 2, (c): Mesh 3. 40

5.8 A simply supported square plate – Convergence test for the strain energy. (a): Mesh 1, (b): Mesh 2, (c): Mesh 3. 41

5.9 A clamped circular plate – Meshes of elements. (a): Mesh 1, (b): Mesh 2, (c): Mesh 3. 44

5.10 A clamped circular plate. (a): Deflection, (b): Deformation of the plate with the mesh of 4×4 elements. 44

5.11 A clamped circular plate. (a): Comparison of the convergence properties between the proposed element and Marc-Mentat, (b): Order of convergence for the relative errors of the center deflection versus the number of side elements. 45

5.12 A clamped cutout square plate. (a): Problem set up, (b): Equivalent model. 46

5.13 A clamped cutout square plate – Contour plot for the deflection. (a): Marc-Mentat, (b): Present. 47

5.14 A clamped cutout plate – Deformation with a mesh of 4×4 proposed element. 47

CHAPTER 1
INTRODUCTION

1.1 General

There are two major plate theories, namely the Kirchhoff and Reissner-Mindlin plate theories. The Kirchhoff plate theory was introduced by Kirchhoff (1850), and this theory can be considered as a two-dimensional extension of the Euler-Bernoulli beam theory. Specifically, shear deformation is neglected in the Kirchhoff plate theory. In contrast, shear deformation is taken into account in the Reissner-Mindlin plate theory, which is similar to the Timoshenko beam theory (Mindlin, 1951; Reissner, 1945). The Kirchhoff plate theory can only be used with thin plates, while the Reissner-Mindlin plate theory is usable with both thin and thick plates.

Analysis of Kirchhoff plate finite elements is still an active field, investigated by researchers who study analysis of civil and mechanical engineering problems. Examples include Peano (1979), Wanji and Cheung (1997), Szilard (2004), Oñate (2013), Cuomo and Greco (2018), and Greco, Cuomo and Contrafatto (2019). To establish the conformity between plate elements, it is required that the transverse and rotational displacements are continuous across the elements. As a result, the C^1 continuity of the transverse displacement between elements is required. Various approaches are attempted to obtain the C^1 continuity of the transverse displacement by considering, for example, incomplete polynomial sequences, mid-side nodes, rectangular elements, and high-order interpolations (Peano, 1979). It is unfortunately difficult to achieve the C^1 continuity in Kirchhoff plate elements. Different interpolation functions have been utilized for different types of nodal degree freedom. In most cases, these different interpolation functions are polynomials. Rectangular plate elements normally contain three or four types of degree of freedom. Three types of degree of freedom normally include a transverse-displacement degree of freedom and two rotational-displacement degrees of freedom. Four types of degree of freedom normally include an additional second-order derivative of the transverse displacement.

1.2 Problem statement

The Reissner-Mindlin plate theory allows the C^0 continuity of the transverse displacement to be used (Neto, Amaro, Roseiro, Cirne & Leal, 2015; Oñate, 2013). This is because, in the Reissner-Mindlin plate theory, the rotational displacements are not the derivatives of the transverse displacement. Therefore, they can be approximated separately from the transverse displacement. This is not true for the Kirchhoff plate theory, where the rotational displacements are the derivatives of the transverse displacement, necessitating the C^1 continuity of the transverse displacement.

Creating Kirchhoff plate elements with the C^0 continuity is straightforward. Kirchhoff plate elements with the C^0 continuity are called non-conforming elements. Since the C^0 continuity is not realistic, the performance of these elements is not excellent. A non-conforming 4-noded rectangular plate element usually has a transverse-displacement degree of freedom and two rotational-displacement degrees of freedom at each node. Kirchhoff plate elements are said to be conforming if the transverse displacement and rotational displacements are continuous across elements. Bogner, Fox and Schmit (1965) used the transverse displacement, two rotational displacements, and second-order derivative of the transverse displacement as the degrees of freedom at each node of a 4-noded rectangular plate element to obtain a conforming element. However, the approach is valid only for rectangular elements.

In the finite element method (FEM), unknown displacement functions are mostly approximated by using standard polynomials. Basically, the unknown displacements are interpolated from displacement qualities at nodes. These interpolation functions are also known as shape functions since they define the deformed shape of the domain being considered. Polynomials are mostly used because they are mathematically easy to manipulate. Polynomials also allow the approximation errors to be systematically controlled. It is worth noting that the higher degrees of polynomials used for interpolation functions are, the more difficult it is to ensure the continuity of the displacement quantities across elements (Szilard, 2004). Polynomials can be written in different forms, such as the monomial, Lagrange, and Bézier forms. The Bézier form of polynomials has been used for geometric design because the Bézier form of polynomials is suitable for representing curves and surfaces. Curves and surfaces written in the Bézier form are known as Bézier curves and surfaces. In contrast to the monomial form, the Bézier form permits easy manipulation of complex functions of curves and surfaces. The limitation of using Bézier curves is that they stop being effective for some highly complex geometries, such as conics and spheres.

At some point in the last decades, rational Bézier and non-uniform rational B-spline (NURBS) curves and surfaces were introduced in computer aid design (CAD) industry. They are proven to be better than polynomials in representing complex geometry, such as conics and spheres. Theoretically, rational Bézier curves and surfaces are special cases of NURBS curves and surfaces (Piegl & Tiller, 1997; Rogers, 2001). Isogeometric analysis (IGA) of structures that uses these CAD functions as interpolation functions has been studied by many researchers (Benson, Bazilevs, Hsu & Hughes, 2010; Cottrell, Hughes & Reali, 2007; De Luycker, Benson, Belytschko, Bazilevs & Hsu, 2011; Fischer, Klassen, Mergheim, Steinmann & Müller, 2011; Hassani, Tavakkoli & Moghadam, 2011; Reali, 2006). This analysis method was introduced by Hughes, Cottrell and Bazilevs (2005), who were inspired by the existing gap between FEM and CAD. In IGA, the same CAD basis functions are used to represent the geometry and the unknown fields. IGA has gained interest from many researchers who study analysis of civil and mechanical engineering structures, such as beams (Li, Zhang & Zheng, 2013), shells (Benson, Bazilevs, Hsu & Hughes, 2010), and structural vibration (Cottrell, Hughes & Reali, 2007).

Plate finite elements, whose geometry is represented by polynomials, always have straight edges. This is because polynomials cannot reproduce complex shapes well. Using CAD functions instead of polynomials allows plates that have complex shapes, such as curved edges, to be represented efficiently. Hence, it can be beneficial if IGA is used to analyze plates. However, one drawback of IGA is that obtaining the C^1 continuity of approximating functions across connecting patches is not straightforward.

In this study, an isogeometric conforming Kirchhoff plate element using rational Bézier basis functions is proposed. In the proposed element, rational Bézier surfaces are used to represent the plate geometry as well as to approximate the unknown displacements. Rational Bézier surfaces allow plates with curved edges to be modeled efficiently. Great care is given to the design of the proposed element to obtain the C^1 continuity of the transverse displacement.

1.3 The objectives of the study

The objectives of this study are as follows:

1. To develop a quadrilateral conforming Kirchhoff plate element by using interpolation functions constructed from bi-cubic rational Bézier basis functions.
2. To use the transverse displacement and rotational displacements, including the rotations about the element edges as the degrees of freedom of the proposed plate element.
3. To investigate the accuracy and efficiency of the proposed plate element by solving some benchmark problems.

1.4 The scope of the study

The scope of the study is as follows:

1. Displacements are small.
2. Materials are homogeneous and linear elastic.

CHAPTER 2
LITERATURE REVIEW

In this chapter, some research works that are relevant to this study are reviewed. The main objective of this study is to create a quadrilateral conforming Kirchhoff plate element by using bi-cubic rational Bézier basis functions. Thus, some works related to beams and plates with various types of interpolation function and the use of CAD functions as interpolation functions are discussed in this chapter.

Melosh (1963), Zienkiewicz and Cheung (1964), Zienkiewicz and Cheung (1965) studied a popular 4-noded rectangular plate element with the use of the transverse displacement and two rotational displacements as the degrees of freedom. Only 12 selected terms from the 15 terms of the complete polynomial of quartic order are used to approximate the transverse displacement. The element violates the continuity of the normal rotation and the second-order derivatives of the transverse displacement at the corners. The element is called a non-conforming 4-noded MZC rectangular element. This element passes the patch test and satisfies the convergence test but its use is limited only to rectangular elements.

Bogner, Fox and Schmit (1965) developed a 4-noded rectangular plate element that uses the transverse displacement, two rotational displacements, and one second-order derivative of the transverse displacement as the degrees of freedom. The bi-cubic Hermitian polynomials are considered as the interpolation functions. With such degrees of freedom and interpolation functions, a conforming element can be obtained. Their conforming element passes the patch test and is more accurate than the MZC element due to the use of more degrees of freedom. However, their element is only applicable to rectangular elements.

Clough and Felippa (1968) studied a fully compatible quadrilateral plate element. The starting point of their work is to create a compatible triangular element first by assembling three sub-elements of a triangle. The complete cubic polynomials are used as the interpolation functions for each sub-element of a triangle. Therefore, the Linear Curvature Compatible Triangle with the use of the transverse displacement, two rotational displacements, and the rotation at the three mid-side nodes about an axis parallel to the side as degrees of freedom (LCCT-12) is achieved. However, one drawback of the LCCT-12 is that the mid-side nodes present the difficulty in mesh generation and require special identification in the development of computer programs. For that reason, the mid-side nodes are eliminated and three new elements, namely LCCT-11, LCCT-10, and LCCT-9 are obtained. Finally, their compatible quadrilateral element with 12 degrees of freedom is developed by assembling the four LCCT-11 elements and applying the static condensation to remove seven internal degrees of freedom of the assemblage. Eventually, their proposed element is considered as the most efficient plate bending element and shows good results for various problems, such as static analyses with and without shear distortion, plate buckling, and plate vibration studies.

Shojaee and Valizadeh (2012) proposed a method that analyzed thin plate problems by utilizing NURBS-based isogeometric analysis. The NURBS basis functions guarantee the inter-element continuity easily for Kirchhoff plate elements. The Lagrange multiplier is used to take care of essential boundary conditions due to non-interpolating nature of NURBS. As a result, the proposed plate element theoretically gives accurate results and resolves the inter-element continuity of thin plate problems.

Mishra and Barik (2017) introduced a new concept aiming to solve the static analysis of arbitrary plates. Their concepts combine NURBS and FEM together since the geometry of arbitrary plates can be represented accurately using NURBS basis functions. However, one drawback of NURBS basis functions is its non-interpolating nature which causes an issue related to essential boundary conditions. From this observation, they choose the classical finite element basis functions for the displacement field in order to take care of essential boundary conditions. Consequently, their proposed method solves many complex shapes of plate elements and provides excellent results in comparison with some existing solutions reviewed in their paper.

Vo (2017) developed a 2D field-consistent rational Bézier beam element for large displacement analysis. In his work, the total Lagrangian description is employed and the kinematics assumptions of the Euler-Bernoulli beam theory are considered in the same way as the work by Nanakorn and Vu (2006). However, the interpolation functions used are different. In the work by Vo (2017), the rational Bézier curve is used to represent the geometry of the beam element. The proposed method in his study is used to solve some benchmark problems and the obtained results are in line with the results by Nanakorn and Vu (2006).

Ranjan and Reddy (2018) proposed a work on nonlinear analysis of straight beams with mixed formulations by using CAD basis functions as interpolation functions. The Euler-Bernoulli and Timoshenko beam theories are employed. Both uniform and non-uniform rational B-spline (NURBS) basis functions are used and the main benefit of using these two classes of functions is to remove shear-locking behavior particularly in the Timoshenko beam theory. Consequently, their proposed approach solves nonlinear beam problems effectively in comparison with the analytical results.

Most recently, a conforming quadrilateral element and two conforming triangular elements are developed, respectively, by Greco, Cuomo and Contrafatto (2019) and Greco, Cuomo and Contrafatto (2019), using CAD basis functions developed by Loop, Schaefer, Ni and Casta (2009). In their works, the transverse displacements of control points are initially considered as the discrete unknowns. After that, these discrete unknowns are transformed into the following degrees of freedom, namely the transverse displacements, the derivatives of the transverse displacement with respect to Cartesian coordinates at the corner nodes, and the normal rotations at two side nodes along each element edge. After transformation and arrangement, their elements consist of 20 degrees of freedom and 15 degrees of freedom for a quadrilateral element and a triangular element, respectively. In addition, in another conforming triangular element by Greco, Cuomo and Contrafatto (2019), the middle transverse displacements along all element sides are added, resulting in 18 degrees of freedom. However, due to the singularity of the basis functions, the rotations at the corners are not explicitly defined. In addition, since these elements are formulated in a curvilinear coordinate system, the formulations are complicated. Nevertheless, their elements present not only the optimal order of convergence but also high accuracy for the analysis of plates with unstructured meshes.

CHAPTER 3

THEORETICAL BACKGROUND

3.1 Kirchhoff plate theory

The Kirchhoff plate theory has been widely used in the analysis of plates. The major kinematic assumptions in the Kirchhoff plate theory are expressed as follows:

- A straight line that is perpendicular to the neutral surface of the plate remains straight and perpendicular to the neutral surface after deformation;
- The thickness of the plate does not change after deformation.

3.1.1 Kinematics

A Cartesian coordinate system, defined by three orthonormal vectors $\mathbf{e}_x - \mathbf{e}_y - \mathbf{e}_z$, is set on the midplane of a plate as shown in Figure 3.1. The vector $\mathbf{e}_z$ is normal to the midplane. The Cartesian coordinates are denoted by x, y, and z, and the displacements along these coordinates are denoted by u, v, and w, respectively. Based on the Kirchhoff plate theory, the displacements are expressed as

$$u = -z\frac{\partial w(x,y)}{\partial x} = -z\theta_x(x,y); \tag{3.1}$$

$$v = -z\frac{\partial w(x,y)}{\partial y} = -z\theta_y(x,y); \tag{3.2}$$

$$w = w(x,y) \tag{3.3}$$

where $\theta_x = \partial w/\partial x$ and $\theta_y = \partial w/\partial y$ are the rotations of a vector normal to the midplane of the plate around the y and x axes, respectively. Positive directions of the rotations, i.e., θ_x and θ_y, are given in Figure 3.1.

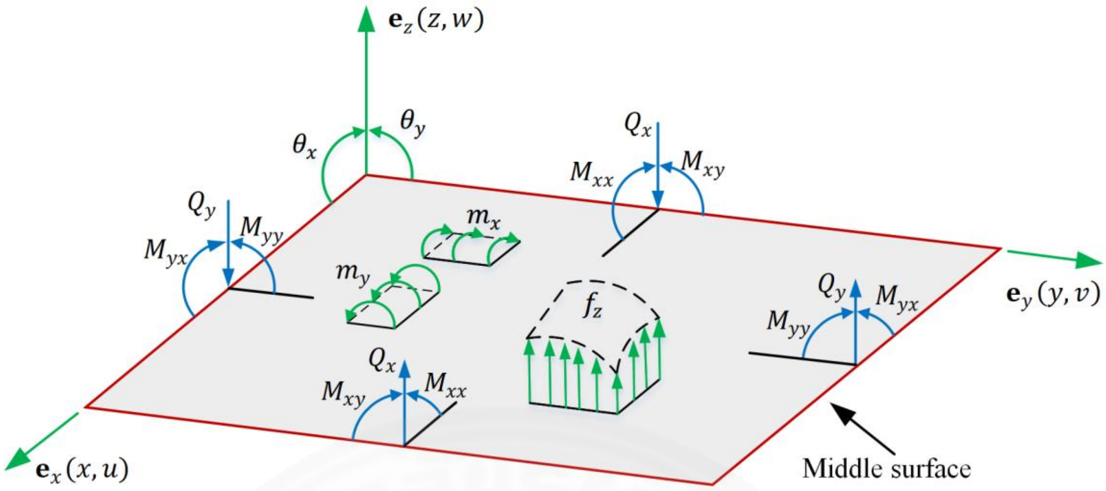

Figure 3.1 Coordinates system of a plate with conventions of internal and external forces.

3.1.2 Strain measurement and stress resultants

In this study, small displacements are considered. As a result, the non-zero strain components are determined as

$$\boldsymbol{\varepsilon} = \begin{bmatrix} \varepsilon_{xx} \\ \varepsilon_{yy} \\ \gamma_{xy} \end{bmatrix} = \begin{bmatrix} -z\dfrac{\partial^2 w}{\partial x^2} & -z\dfrac{\partial^2 w}{\partial y^2} & -2z\dfrac{\partial^2 w}{\partial x \partial y} \end{bmatrix}^{\mathrm{T}} = -z\boldsymbol{\kappa} \tag{3.4}$$

where $\boldsymbol{\kappa}$ is the bending curvature vector of the midplane of the plate, defined as

$$\boldsymbol{\kappa} = \begin{bmatrix} \dfrac{\partial^2 w}{\partial x^2} & \dfrac{\partial^2 w}{\partial y^2} & 2\dfrac{\partial^2 w}{\partial x \partial y} \end{bmatrix}^{\mathrm{T}}. \tag{3.5}$$

Since the linear elastic material is considered, the non-zero stress components can be determined as

$$\boldsymbol{\sigma} = \begin{bmatrix} \sigma_{xx} \\ \sigma_{yy} \\ \tau_{xy} \end{bmatrix} = \frac{E}{1-\nu^2}\begin{bmatrix} 1 & \nu & 0 \\ \nu & 1 & 0 \\ 0 & 0 & \dfrac{1-\nu}{2} \end{bmatrix}\begin{bmatrix} \varepsilon_{xx} \\ \varepsilon_{yy} \\ \gamma_{xy} \end{bmatrix} = \mathbf{D}\boldsymbol{\varepsilon} = -z\mathbf{D}\boldsymbol{\kappa}. \tag{3.6}$$

Here, E and ν are Young's modulus and Poisson's ratio, respectively. The matrix $\mathbf{D}$ is defined as

$$\mathbf{D} = \frac{E}{1-\nu^2}\begin{bmatrix} 1 & \nu & 0 \\ \nu & 1 & 0 \\ 0 & 0 & \dfrac{1-\nu}{2} \end{bmatrix}. \tag{3.7}$$

The stress resultants are defined as the integration of the stress over the thickness, i.e.

$$\mathbf{M} = \begin{bmatrix} M_{xx} \\ M_{yy} \\ M_{xy} \end{bmatrix} = \int_{-h/2}^{h/2} \boldsymbol{\sigma} z \,\mathrm{d}z = -\int_{-h/2}^{h/2} z^2 \,\mathrm{d}z \mathbf{D}\boldsymbol{\kappa} = -\frac{h^3}{12}\mathbf{D}\boldsymbol{\kappa} \tag{3.8}$$

where h denotes the thickness of the plate. For the Kirchhoff plate theory, resultant shear forces, i.e., Q_x and Q_y, are not determined by the integrations of the stress components. Instead, they are computed from equilibrium conditions (Oñate, 2013). The sign conventions for the moments and shear forces are given in Figure 3.1.

3.1.3 Virtual work equation for a Kirchhoff plate

The virtual work equation is written as

$$\delta W_{int} - \delta W_{ext} = 0 \tag{3.9}$$

where δW_{int} is the internal virtual work, and δW_{ext} is the external virtual work.

The internal virtual work δW_{int} is expressed as

$$\delta W_{int} = \int_V \delta \boldsymbol{\varepsilon}^{\mathrm{T}} \boldsymbol{\sigma} \,\mathrm{d}V. \tag{3.10}$$

Here, V denotes the plate volume. Using Equation (3.4) and Equation (3.8) in Equation (3.10) yields

$$\delta W_{int} = \int_V \delta \boldsymbol{\varepsilon}^{\mathrm{T}} \boldsymbol{\sigma} \,\mathrm{d}V = -\int_A \delta \boldsymbol{\kappa}^{\mathrm{T}} \mathbf{M} \,\mathrm{d}A = \frac{h^3}{12}\int_A \delta \boldsymbol{\kappa}^{\mathrm{T}} \mathbf{D}\boldsymbol{\kappa} \,\mathrm{d}A \tag{3.11}$$

where A denotes the area of the midplane surface. On the other hand, the external virtual work δW_{ext} is determined as

$$\delta W_{ext} = \int_A \delta \mathbf{u}^{\mathrm{T}} \mathbf{f} \, dA \tag{3.12}$$

where $\mathbf{u} = [w \quad \theta_x \quad \theta_y]^{\mathrm{T}}$ is the displacement vector of the middle surface. In addition, $\mathbf{f} = [f_z \quad m_x \quad m_y]^{\mathrm{T}}$ is the distributed load vector, where f_z is the distributed force, m_x and m_y are the distributed moments. The sign conventions for the external loads are shown in Figure 3.1.

3.2 Non-conforming 4-noded MZC rectangular plate element

As mentioned previously, a non-conforming 4-noded rectangular element has been developed by Melosh (1963), Zienkiewicz and Cheung (1964), and Zienkiewicz and Cheung (1965). There are three degrees of freedom namely the transverse displacement and two rotational displacements at each corner as shown in Figure 3.2. The quartic polynomial is used to approximate the displacement field but only 12 terms are considered in order to match the number of degrees of freedom. Therefore, the form of the displacement approximation is

$$\begin{aligned} w = a_1 + a_2 x + a_3 y + a_4 x^2 + a_5 xy + a_6 y + a_7 x^3 + a_8 x^2 y + a_9 xy^2 \\ + a_{10} y^3 + a_{11} x^3 y + a_{12} xy^3. \end{aligned} \tag{3.13}$$

Let $\mathbf{a}$ be a vector containing the unknown coefficients and $\mathbf{A}$ be a vector with the selected 12 terms of the quartic polynomials. They are defined as

$$\mathbf{a} = [a_1 \quad a_2 \quad a_3 \quad \cdots \quad a_{10} \quad a_{11} \quad a_{12}]^{\mathrm{T}}; \tag{3.14}$$

$$\mathbf{A} = [1 \quad x \quad y \quad \cdots \quad y^3 \quad x^3 y \quad xy^3]. \tag{3.15}$$

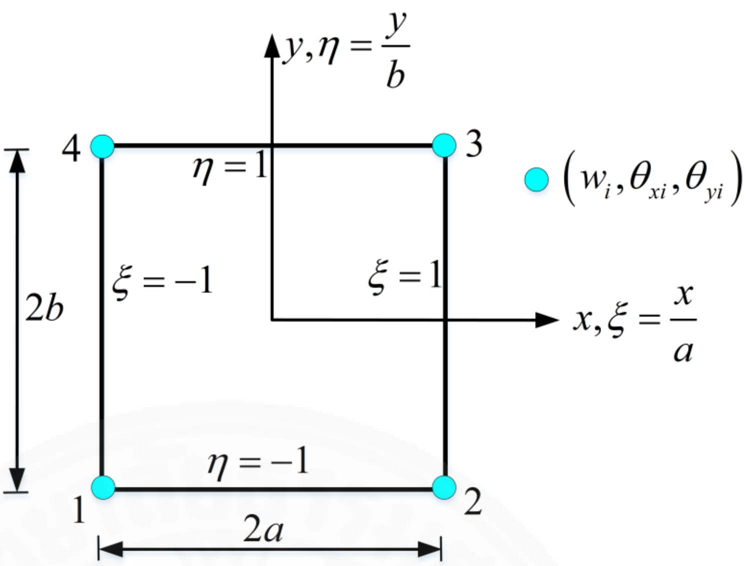

Figure 3.2 Non-conforming 4-noded MZC.

From Equation (3.14) and Equation (3.15), Equation (3.13) is rewritten as

$$w = \mathbf{Aa}. \tag{3.16}$$

The relation between the nodal degrees of freedom and unknown coefficients is obtained at the four nodes as

$$\mathbf{u} = \begin{bmatrix} w_1 \\ \partial w_1/\partial x \\ \partial w_1/\partial y \\ \vdots \\ w_4 \\ \partial w_4/\partial x \\ \partial w_4/\partial y \end{bmatrix} = \mathbf{Xa} \tag{3.17}$$

where

$$\mathbf{u} = [w_1 \quad \theta_{x1} \quad \theta_{y1} \quad \cdots \quad w_4 \quad \theta_{x4} \quad \theta_{y4}]^{\mathrm{T}}. \tag{3.18}$$

Since the matrix **X** is a square matrix, it follows that

$$\mathbf{a} = \mathbf{X}^{-1}\mathbf{u}. \tag{3.19}$$

Substituting Equation (3.19) into Equation (3.16), the displacement field can be expressed in terms of the nodal degrees of freedom as

$$w = \mathbf{A}\mathbf{X}^{-1}\mathbf{u}. \tag{3.20}$$

Note that the stiffness matrix equations can be obtained by substituting Equation (3.20) into Equations (3.11) and (3.12). However, this process is not straightforward and costly. Later, Melosh (1963) developed explicit forms for the shape functions of the four nodes shown in Figure 3.2. They are given by

$$N_i = \frac{(1+\xi_i\xi)(1+\eta_i\eta)(2+\xi_i\xi+\eta_i\eta-\xi^2-\eta^2)}{8}; \tag{3.21}$$

$$\bar{N}_i = \frac{a(\xi^2-1)(\xi+\xi_i)(1+\eta_i\eta)}{8}; \tag{3.22}$$

$$\bar{\bar{N}}_i = \frac{b(\eta^2-1)(\eta+\eta_i)(1+\xi_i\xi)}{8} \tag{3.23}$$

where N_i, $\bar{N}_i$, and $\bar{\bar{N}}_i$ are, respectively, the shape functions of the displacement, the rotations around y and x axes at node i. They are being considered in the natural coordinates, which vary between -1 and 1 horizontally and vertically. Therefore, the displacement field becomes

$$w = \sum_{i=1}^{4}\left[N_i w_i + \bar{N}_i\theta_{xi} + \bar{\bar{N}}_i\theta_{yi}\right] = \mathbf{N}\mathbf{u} \tag{3.24}$$

where

$$\mathbf{N} = [\mathbf{N}_1 \quad \mathbf{N}_2 \quad \mathbf{N}_3 \quad \mathbf{N}_4]; \qquad \mathbf{u} = [\mathbf{u}_1 \quad \mathbf{u}_2 \quad \mathbf{u}_3 \quad \mathbf{u}_4]^{\mathrm{T}}; \tag{3.25}$$

$$\mathbf{N}_i = \left[N_i \quad \bar{N}_i \quad \bar{\bar{N}}_i\right]; \qquad \mathbf{u}_i = [w_i \quad \theta_{xi} \quad \theta_{yi}]^{\mathrm{T}}. \tag{3.26}$$

Based on Equation (3.24), the bending curvature matrix is written as

$$\boldsymbol{\kappa} = \sum_{i=1}^{4}\mathbf{B}_i\mathbf{u}_i = \mathbf{B}\mathbf{u} \tag{3.27}$$

where

$$\mathbf{B} = [\mathbf{B}_1 \quad \mathbf{B}_2 \quad \mathbf{B}_3 \quad \mathbf{B}_4]; \tag{3.28}$$

$$\mathbf{B}_i = \begin{bmatrix} \dfrac{\partial^2 N_i}{\partial x^2} & \dfrac{\partial^2 \overline{N}_i}{\partial x^2} & \dfrac{\partial^2 \overline{\overline{N}}_i}{\partial x^2} \\ \dfrac{\partial^2 N_i}{\partial y^2} & \dfrac{\partial^2 \overline{N}_i}{\partial y^2} & \dfrac{\partial^2 \overline{\overline{N}}_i}{\partial y^2} \\ 2\dfrac{\partial^2 N_i}{\partial x \partial y} & 2\dfrac{\partial^2 \overline{N}_i}{\partial x \partial y} & 2\dfrac{\partial^2 \overline{\overline{N}}_i}{\partial x \partial y} \end{bmatrix}. \tag{3.29}$$

The second-order derivatives of the shape functions are computed based on the relationship between the Cartesian coordinates x, y and the natural coordinates ξ, η. The detailed derivatives of the shape functions can be found in the work by Oñate (2013). Substituting Equation (3.24) and Equation (3.27) into Equations (3.11)-(3.12) gives the compact form of the virtual work equation, i.e.

$$\mathbf{Ku} = \mathbf{F} \tag{3.30}$$

where the stiffness matrix **K** and force vector **F** are defined as

$$\mathbf{K} = \frac{h^3}{12}\int_A \mathbf{B}^{\mathrm{T}}\mathbf{D}\mathbf{B}\, d\mathrm{A}; \tag{3.31}$$

$$\mathbf{F} = [\mathbf{F}_1 \quad \mathbf{F}_2 \quad \mathbf{F}_3 \quad \mathbf{F}_4]^{\mathrm{T}}; \tag{3.32}$$

$$\mathbf{F}_i = \begin{bmatrix} f_{zi} \\ m_{xi} \\ m_{yi} \end{bmatrix} = \int_A \begin{bmatrix} N_i & \dfrac{\partial N_i}{\partial x} & \dfrac{\partial N_i}{\partial y} \\ \overline{N}_i & \dfrac{\partial \overline{N}_i}{\partial x} & \dfrac{\partial \overline{N}_i}{\partial y} \\ \overline{\overline{N}}_i & \dfrac{\partial \overline{\overline{N}}_i}{\partial x} & \dfrac{\partial \overline{\overline{N}}_i}{\partial y} \end{bmatrix} \mathbf{f}\, d\mathrm{A}. \tag{3.33}$$

Equation (3.30) is the stiffness matrix equation for the MZC rectangular plate element.

Consider two connecting elements shown in Figure 3.3. The first element has nodes 1, 2, 4, and 3, while the second element has nodes 3, 4, 6, and 5 as shown in the figure. The shape functions of the two adjacent elements are computed based on Equation (3.20). Set all nodal degrees of freedom to zero except for the rotation around y axis at node 5, which is set to 1 as shown in Figure 3.3. Figure 3.3 (a) and Figure 3.3 (b) show that the displacement and the rotation around y axis are continuous everywhere. However, the rotation around x axis is not continuous across the two elements as shown in Figure 3.3 (c). Therefore, the MZC plate element does not satisfy the necessary continuity conditions and is a non-conforming element.

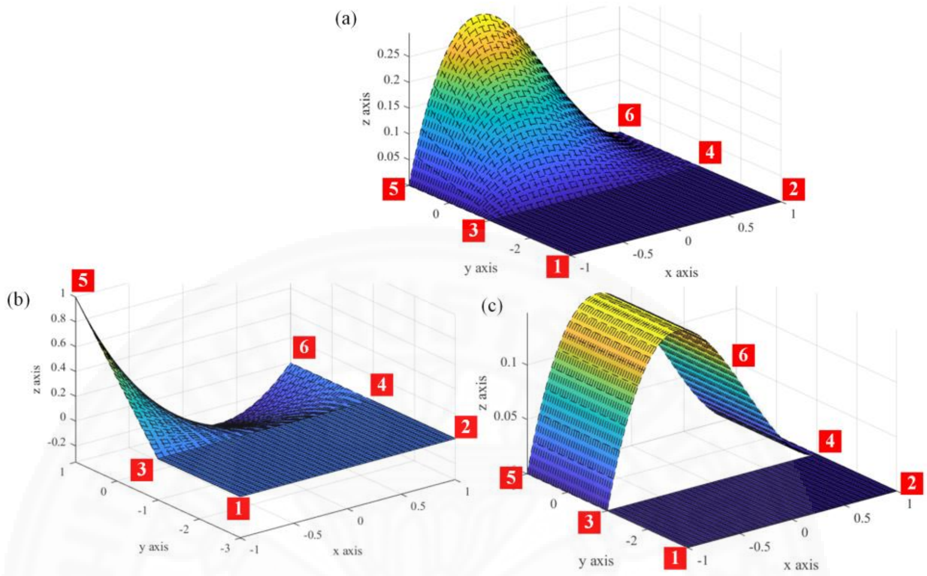

Figure 3.3 Non-conforming 4-noded MZC (a): displacement, (b): rotation around y axis, and (c): rotation around x axis.

3.3 Conforming element 4-noded BFS rectangular element

As aforementioned , it is impossible to obtain a conforming rectangular element with only the use of the displacement and two rotational displacements as degrees of freedom. Bogner, Fox and Schmit (1965) developed a BFS rectangular element by adding a second-order derivative of the transverse displacement as an additional degree of freedom. Therefore, the total number of degrees of freedom is 16 as shown in Figure 3.4. Bi-cubic Hermite polynomials are used to construct their interpolation functions (Oñate, 2013). Develop 1D cubic Hermite polynomials along ξ and η of each element side, for example at node 1 and node 2, as

- Along ξ axis

$$N_{\xi 1} = \frac{1}{4}(2 - 3\xi + \xi^3); \tag{3.34}$$

$$N_{\xi 2} = \frac{1}{4}(2 + 3\xi - \xi^3); \tag{3.35}$$

$$\bar{N}_{\xi 1} = \frac{1}{4}(1 - \xi - \xi^2 + \xi^3); \tag{3.36}$$

$$\bar{N}_{\xi 2} = \frac{1}{4}(-1 - \xi + \xi^2 + \xi^3). \tag{3.37}$$

- Along η axis

$$N_{\eta 1} = \frac{1}{4}(2 - 3\eta + \eta^3); \tag{3.38}$$

$$N_{\eta 2} = \frac{1}{4}(2 + 3\eta - \eta^3); \tag{3.39}$$

$$\bar{N}_{\eta 1} = \frac{1}{4}(1 - \eta - \eta^2 + \eta^3); \tag{3.40}$$

$$\bar{N}_{\eta 2} = \frac{1}{4}(-1 - \eta + \eta^2 + \eta^3). \tag{3.41}$$

The shape functions of the displacement, the rotational displacements and the second-order derivative of the displacement are then written using the polynomials in Equations (3.34)-(3.41) as

$$\mathbf{N}_w = [N_{\xi 1}N_{\eta 1} \quad N_{\xi 2}N_{\eta 1} \quad N_{\xi 2}N_{\eta 2} \quad N_{\xi 1}N_{\eta 2}]; \tag{3.42}$$

$$\mathbf{N}_{\theta_x} = \left[\bar{N}_{\xi 1}N_{\eta 1} \quad \bar{N}_{\xi 2}N_{\eta 1} \quad \bar{N}_{\xi 2}N_{\eta 2} \quad \bar{N}_{\xi 1}N_{\eta 2}\right]; \tag{3.43}$$

$$\mathbf{N}_{\theta_y} = \left[N_{\xi 1}\bar{N}_{\eta 1} \quad N_{\xi 2}\bar{N}_{\eta 1} \quad N_{\xi 2}\bar{N}_{\eta 2} \quad N_{\xi 1}\bar{N}_{\eta 2}\right]; \tag{3.44}$$

$$\mathbf{N}_{\theta_{xy}} = \left[\bar{N}_{\xi 1}\bar{N}_{\eta 1} \quad \bar{N}_{\xi 2}\bar{N}_{\eta 1} \quad \bar{N}_{\xi 2}\bar{N}_{\eta 2} \quad \bar{N}_{\xi 1}\bar{N}_{\eta 2}\right]. \tag{3.45}$$

The shape function matrix $\mathbf{N}$ and the displacement vector $\mathbf{u}$ are then written as

$$\mathbf{N} = \left[\mathbf{N}_w \quad \mathbf{N}_{\theta_x} \quad \mathbf{N}_{\theta_y} \quad \mathbf{N}_{\theta_{xy}}\right]; \tag{3.46}$$

$$\mathbf{u} = [w_1 \quad w_2 \quad w_3 \quad w_4 \quad \cdots \quad \theta_{xy1} \quad \theta_{xy2} \quad \theta_{xy3} \quad \theta_{xy4}]^{\mathrm{T}}. \tag{3.47}$$

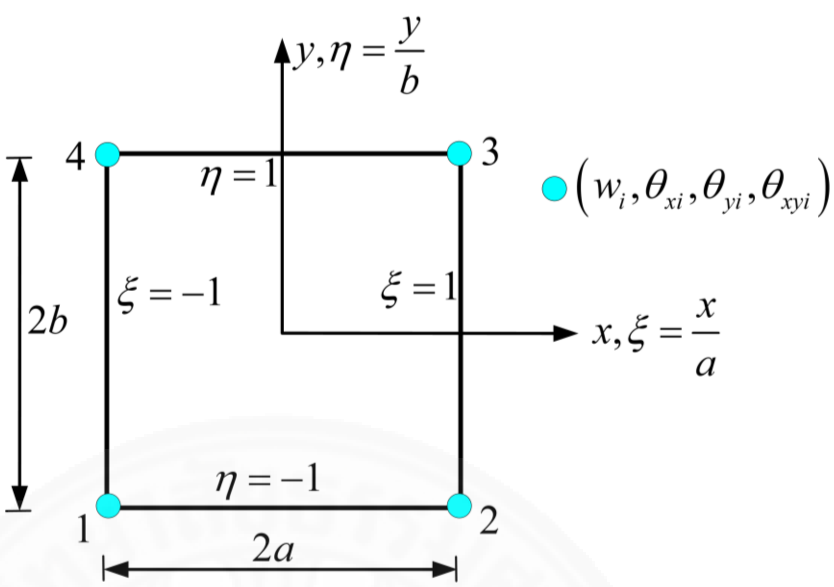

Figure 3.4 Conforming element 4-noded BFS.

To show the conformity of the BFS rectangular element, a similar test to the one in section 3.2 is used. Figure 3.5 (a), (b), and (c) show the plots of the displacement, the rotation around y axis and the rotation around x axis, respectively. All the three fields are continuous across the two elements. Although the BFS rectangular element is a conforming element, the limitation of this element is that it stops being effective when it is distorted.

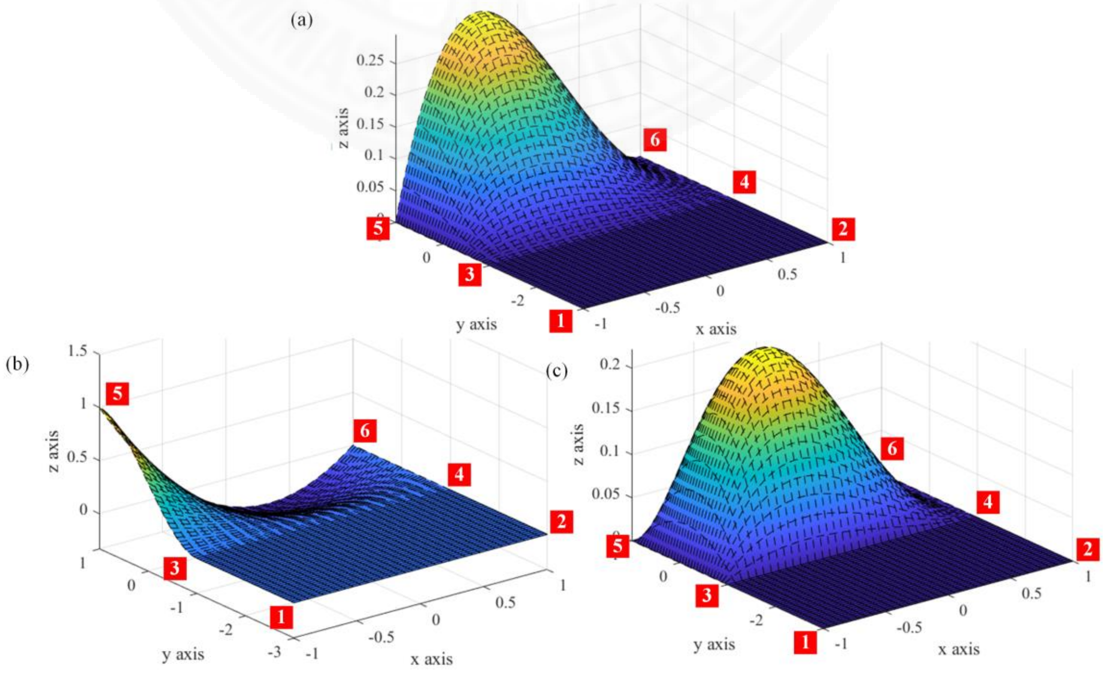

Figure 3.5 Conforming element 4-noded BFS. (a): displacement, (b): rotation around y axis, and (c): rotation around x axis.

3.4 Bernstein polynomials and rational Bézier surfaces

3.4.1 Bézier curves

As mentioned previously, polynomials can be written in various forms, e.g., the monomial form, the Lagrangian form, and the Bézier form. The monomial form of p-degree 2D curves is given as

$$\mathbf{C}(\xi) = \sum_{i=0}^{p} \xi^i \mathbf{P}_i \tag{3.48}$$

where ξ is the independent variable, $\mathbf{C}(\xi) \in \mathbb{R}^2$, and $\mathbf{P}_i \in \mathbb{R}^2$. Although the monomial form is straightforward to understand and manipulate, they are not a suitable candidate for representing curves and surfaces. To represent curves and surfaces, alternative forms of polynomial curves are required. Polynomials can be written in terms of Bernstein polynomials or Bernstein basis functions $B_{i,p}(\xi)$, given as

$$B_{i,p}(\xi) = \binom{p}{i-1} \xi^{i-1}(1-\xi)^{p-i+1} \tag{3.49}$$

where $\binom{p}{i-1}$ is a binomial coefficient. Each Bernstein basis function $B_{i,p}(\xi)$ in Equation (3.49) is valid over the interval $[0,1]$. More importantly, a Bernstein basis function can also be defined on an arbitrary interval $[a, b]$ as

$$B_{i,p}(\xi) = \binom{p}{i-1} \left(\frac{\xi - a}{b - a}\right)^{i-1} \left(\frac{b - \xi}{b - a}\right)^{p-i+1}. \tag{3.50}$$

Some important properties of the Bernstein basis functions over an interval $[a, b]$ are as follows:

- Linear independence

$$\sum_{i=1}^{p+1} c_i B_{i,p}(\xi) = 0 \leftrightarrow c_i = 0, \forall \xi \in [a, b]; \tag{3.51}$$

- Partition of unity

$$\sum_{i=1}^{p+1} B_{i,p}(\xi) = 1, \forall \xi \in [a, b]; \tag{3.52}$$

- Non-negativity

$$B_{i,p}(\xi) \geq 0, \forall \xi \in [a, b], i = 1, \dots, (p+1). \tag{3.53}$$

The cubic Bernstein basis functions over the interval $[0,1]$ are visualized in Figure 3.6. Note that all the Bernstein basis functions are positive.

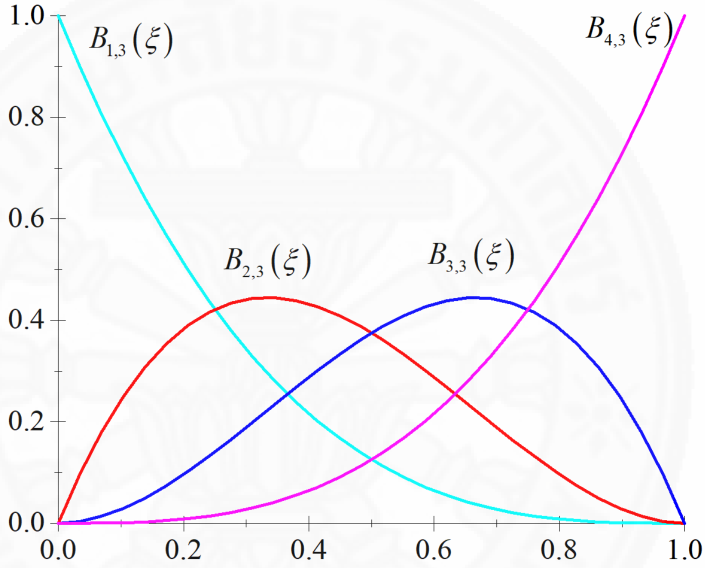

Figure 3.6 Cubic Bernstein basis functions.

A Bézier curve is a linear combination of $p+1$ Bernstein basis functions, expressed as

$$\mathbf{C}(\xi) = \sum_{i=1}^{p+1} B_{i,p}(\xi)\mathbf{P}_i \tag{3.54}$$

where $\mathbf{C}(\xi) \in \mathbb{R}^2$, and $\mathbf{P}_i \in \mathbb{R}^2$. Note that $\mathbf{P}_i$ is a vector of Bézier control point i. It is straightforward to construct the Bézier curves defined in Equation (3.54) by providing the desired degree p and the location of the control points. The cubic Bézier curve is depicted in Figure 3.7.

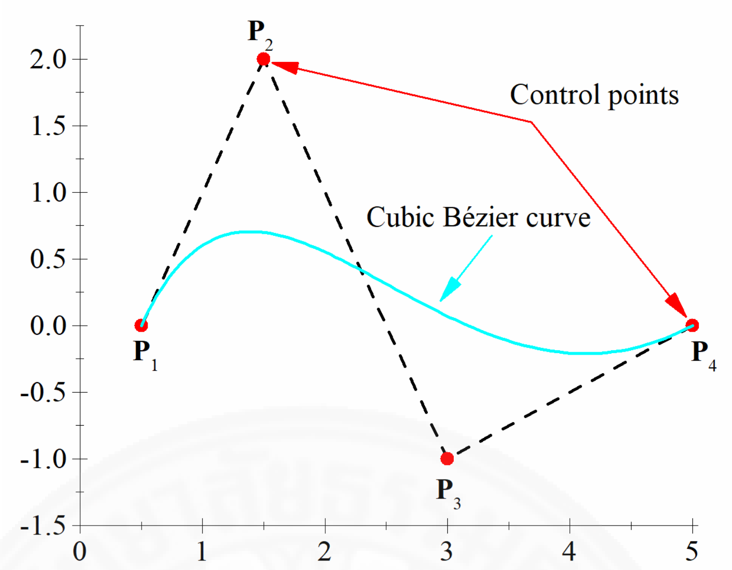

Figure 3.7 Cubic Bézier curve.

3.4.2 Rational Bézier surfaces

As aforementioned, polynomials, including Bézier functions, are not effective in representing complex geometries, such as conic, sphere sections. Functions constructed from rational Bézier basis functions are among those that can effectively represent complex geometries. Rational Bézier basis functions are defined as

$$R_{i,p}(\xi) = \frac{B_{i,p}(\xi)W_i}{\sum_{j=1}^{p+1} B_{j,p}(\xi)W_j} \tag{3.55}$$

where W_i is the i^{th} positive weight. A two-dimensional rational Bézier curve is parametrically expressed as

$$\mathbf{C}(\xi) = \sum_{i=1}^{p+1} R_{i,p}(\xi)\mathbf{P}_i \tag{3.56}$$

where $\mathbf{C}(\xi) \in \mathbb{R}^2$, and $\mathbf{P}_i \in \mathbb{R}^2$.

To demonstrate the effectiveness of using rational Bézier curves for geometrical design, quadratic Bézier and quadratic rational Bézier curves are used to represent a full circle in Figure 3.8. The circle is better represented by the rational Bézier curve.

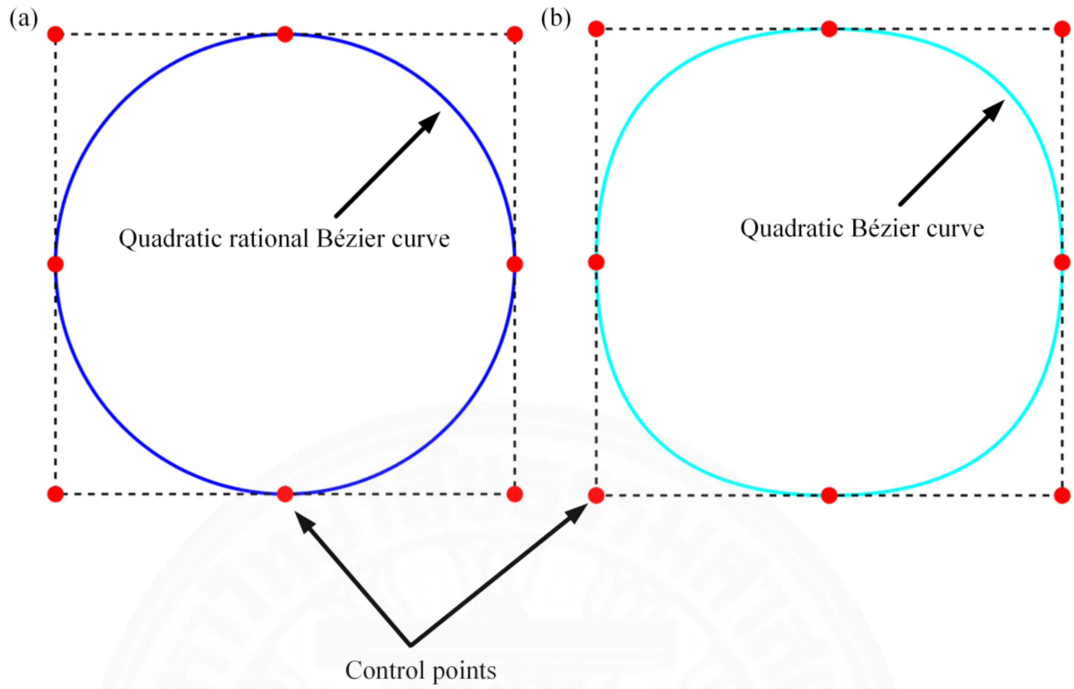

Figure 3.8 Representation of a circle by quadratic Bézier and quadratic rational Bézier curves. (a): quadratic rational Bézier curves, (b): quadratic Bézier curves

Denote a bidirectional net of control points by $\mathbf{P}_{i,j}$, where $i = 1,2, \ldots, p+1, j = 1,2, \ldots, q+1$. Note that p and q are the degrees of polynomials. A rational Bézier surface is written as the product of two univariate rational Bézier basis functions, i.e.

$$\mathbf{S}(\xi, \eta) = \sum_{i=1}^{p+1} \sum_{j=1}^{q+1} R_{i,p}(\xi) R_{j,q}(\eta) \mathbf{P}_{i,j}. \tag{3.57}$$

Here are some major properties of rational Bézier basis functions and surfaces:

- Partition of unity

$$\sum_{i=1}^{p+1} \sum_{j=1}^{q+1} R_{i,p}(\xi) R_{j,q}(\eta) = \left(\sum_{i=1}^{p+1} R_{i,p}(\xi) \right) \left(\sum_{j=1}^{q+1} R_{j,q}(\eta) \right) = 1. \tag{3.58}$$

- Nonnegativity

$$\left(\sum_{i=1}^{p+1} R_{i,p}\,(\xi)\right) \geq 0; \tag{3.59}$$

$$\left(\sum_{j=1}^{q+1} R_{j,q}\,(\eta)\right) \geq 0; \forall(\xi,\eta). \tag{3.60}$$

- Rational Bézier surfaces are interpolated at the four corner control points.

The global index of the control points and its associated basis functions is introduced as

$$I = (p+1)(j-1) + i. \tag{3.61}$$

By referring to Equation (3.61), Equation (3.57) is simplified here as

$$\mathbf{S}(\xi,\eta) = \sum_{I=1}^{(p+1)\times(q+1)} R_I\,(\xi,\eta)\mathbf{P}_I \tag{3.62}$$

where $\mathbf{P}_I = \mathbf{P}_{i,j}$ and $R_I(\xi,\eta) = R_{i,p}(\xi)R_{j,q}(\eta)$.

To demonstrate how rational Bézier surfaces can be used to represent plates with curved boundaries, a flat surface with circular boundaries is constructed by using rational Bézier surfaces in Figure 3.9. It can be seen from the figure that the circular boundaries are perfectly represented. This example clearly shows the strong point of using rational Bézier surfaces to represent plates with curved boundaries. In this study, rational Bézier surfaces are used to represent the geometry of the proposed element.

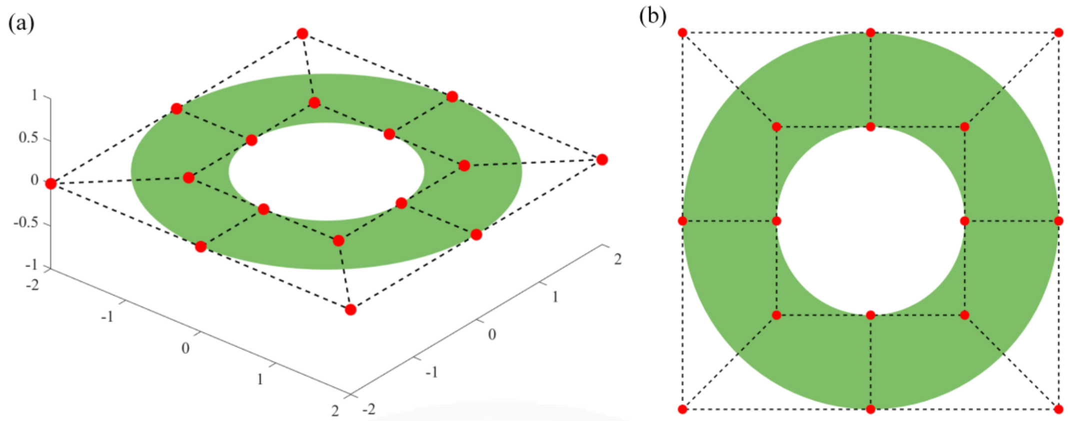

Figure 3.9 A flat surface with curved boundaries represented by a rational Bézier surface.

CHAPTER 4
THE BI-CUBIC BÉZIER QUADRILATERAL CONFORMING PLATE ELEMENT

4.1 Approximations of the geometry and deflection of the plate element

The initial geometry and deflection of the plate element proposed in this study are represented by bi-cubic rational Bézier surfaces with 16 control points. The numbering of the control points is shown in Figure 4.1, where the element is, as an example, used to represent a quarter of an annulus. Based on the 16 control points, the initial geometry of an arbitrary plate element is expressed as

$$\mathbf{S}(\xi,\eta) = \sum_{I=1}^{16} R_I(\xi,\eta)\mathbf{P}_I \tag{4.1}$$

where $\mathbf{S}(\xi,\eta)$ is the initial midplane of a proposed plate element, $\mathbf{P}_I \in \mathbb{R}^3$ is the control point I, and $R_I(\xi,\eta)$ is a bi-cubic rational Bézier basis function.

The deflection w of the plate is approximated in the same manner as

$$w(\xi,\eta) = \sum_{I=1}^{16} R_I(\xi,\eta) d_I \tag{4.2}$$

where d_I is the deflection control variable of control point $\mathbf{P}_I$. The vector of control variables $\mathbf{d}$ is defined as

$$\mathbf{d} = [d_1 \quad d_2 \quad \dots \quad d_{16}]^{\mathrm{T}}. \tag{4.3}$$

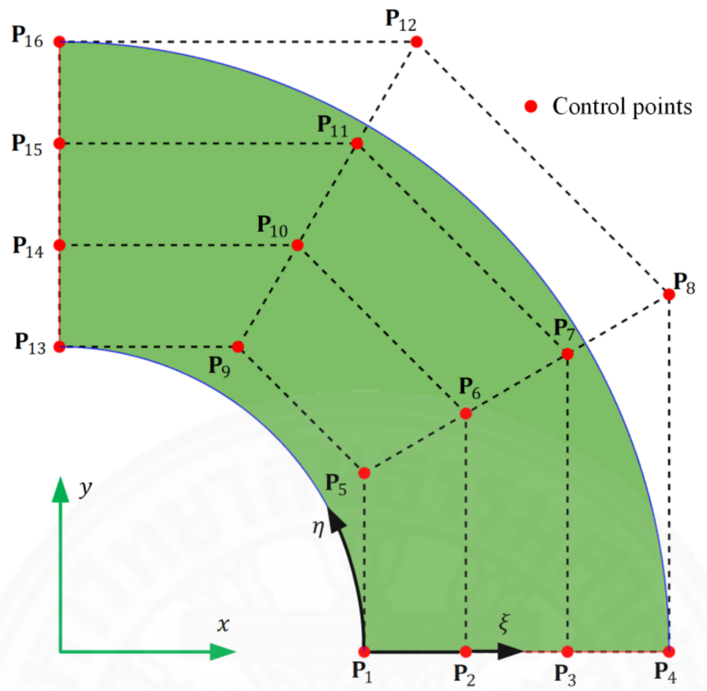

Figure 4.1 Bi-cubic rational Bézier representation of a quarter of an annulus.

4.2 The finite element equation and unique transformation

Substituting Equation (4.2) into Equation (3.11) and Equation (3.12) gives the finite element equation, i.e.

$$\mathbf{Kd} = \mathbf{F} \tag{4.4}$$

where the stiffness matrix **K** and the force vector **F** are given by

$$\mathbf{K} = \frac{h^3}{12}\int_A \mathbf{B}^{\mathrm{T}}\mathbf{D}\mathbf{B}\, dA; \tag{4.5}$$

$$\mathbf{F} = \int_A \mathbf{R}^{\mathrm{T}}\mathbf{f}\, dA. \tag{4.6}$$

Here,

$$\mathbf{B}=\begin{bmatrix}\dfrac{\partial^2 R_1}{\partial x^2} & \dfrac{\partial^2 R_2}{\partial x^2} & \cdots & \dfrac{\partial^2 R_{16}}{\partial x^2}\\ \dfrac{\partial^2 R_1}{\partial y^2} & \dfrac{\partial^2 R_2}{\partial y^2} & \cdots & \dfrac{\partial^2 R_{16}}{\partial y^2}\\ 2\dfrac{\partial^2 R_1}{\partial x\partial y} & 2\dfrac{\partial^2 R_2}{\partial x\partial y} & \cdots & 2\dfrac{\partial^2 R_{16}}{\partial x\partial y}\end{bmatrix}; \tag{4.7}$$

$$\mathbf{R}=\begin{bmatrix}R_1(\xi,\eta) & R_2(\xi,\eta) & \cdots & R_{16}(\xi,\eta)\\ \dfrac{\partial R_1(\xi,\eta)}{\partial x} & \dfrac{\partial R_2(\xi,\eta)}{\partial x} & \cdots & \dfrac{\partial R_{16}(\xi,\eta)}{\partial x}\\ \dfrac{\partial R_1(\xi,\eta)}{\partial y} & \dfrac{\partial R_2(\xi,\eta)}{\partial y} & \cdots & \dfrac{\partial R_{16}(\xi,\eta)}{\partial y}\end{bmatrix}. \tag{4.8}$$

The rational Bézier basis functions are parameterized by the parameters ξ and η. The first and second-order derivatives of the rational Bézier basis functions with respect to the coordinates x and y are given as

$$\begin{bmatrix}\dfrac{\partial R_I}{\partial \xi}\\ \dfrac{\partial R_I}{\partial \eta}\end{bmatrix}=\begin{bmatrix}\dfrac{\partial x}{\partial \xi} & \dfrac{\partial y}{\partial \xi}\\ \dfrac{\partial x}{\partial \eta} & \dfrac{\partial y}{\partial \eta}\end{bmatrix}\begin{bmatrix}\dfrac{\partial R_I}{\partial x}\\ \dfrac{\partial R_I}{\partial y}\end{bmatrix}\rightarrow\begin{bmatrix}\dfrac{\partial R_I}{\partial x}\\ \dfrac{\partial R_I}{\partial y}\end{bmatrix}=\begin{bmatrix}\dfrac{\partial x}{\partial \xi} & \dfrac{\partial y}{\partial \xi}\\ \dfrac{\partial x}{\partial \eta} & \dfrac{\partial y}{\partial \eta}\end{bmatrix}^{-1}\begin{bmatrix}\dfrac{\partial R_I}{\partial \xi}\\ \dfrac{\partial R_I}{\partial \eta}\end{bmatrix}. \tag{4.9}$$

The Jacobian matrix $\mathbf{J}$ is defined as

$$\mathbf{J}=\begin{bmatrix}\dfrac{\partial x}{\partial \xi} & \dfrac{\partial y}{\partial \xi}\\ \dfrac{\partial x}{\partial \eta} & \dfrac{\partial y}{\partial \eta}\end{bmatrix}. \tag{4.10}$$

The second-order derivatives of the rational Bézier basis functions are determined as

$$\begin{bmatrix}\dfrac{\partial^2 R_I}{\partial x^2}\\ \dfrac{\partial^2 R_I}{\partial y^2}\\ \dfrac{\partial^2 R_I}{\partial x\partial y}\end{bmatrix}=\begin{bmatrix}\left(\dfrac{\partial x}{\partial \xi}\right)^2 & \left(\dfrac{\partial y}{\partial \xi}\right)^2 & 2\dfrac{\partial x}{\partial \xi}\dfrac{\partial y}{\partial \xi}\\ \left(\dfrac{\partial x}{\partial \eta}\right)^2 & \left(\dfrac{\partial y}{\partial \eta}\right)^2 & 2\dfrac{\partial x}{\partial \eta}\dfrac{\partial y}{\partial \eta}\\ \dfrac{\partial x}{\partial \xi}\dfrac{\partial x}{\partial \eta} & \dfrac{\partial y}{\partial \xi}\dfrac{\partial y}{\partial \eta} & \dfrac{\partial x}{\partial \xi}\dfrac{\partial y}{\partial \eta}+\dfrac{\partial x}{\partial \eta}\dfrac{\partial y}{\partial \xi}\end{bmatrix}^{-1}\times \tag{4.11}$$

$$\left(\begin{bmatrix}\dfrac{\partial^2 R_I}{\partial \xi^2}\\ \dfrac{\partial^2 R_I}{\partial \eta^2}\\ \dfrac{\partial^2 R_I}{\partial \xi \partial \eta}\end{bmatrix} - \begin{bmatrix}\dfrac{\partial^2 x}{\partial \xi^2} & \dfrac{\partial^2 y}{\partial \xi^2}\\ \dfrac{\partial^2 x}{\partial \eta^2} & \dfrac{\partial^2 y}{\partial \eta^2}\\ \dfrac{\partial^2 x}{\partial \xi \partial \eta} & \dfrac{\partial^2 y}{\partial \xi \partial \eta}\end{bmatrix}\begin{bmatrix}\dfrac{\partial R_I}{\partial x}\\ \dfrac{\partial R_I}{\partial y}\end{bmatrix}\right).$$

4.2.1 Conforming plate element

To satisfy the conformity between elements, it is beneficial to use the normal rotations along the element sides as degrees of freedom. In this study, a normal rotation is the rotation of a vector that is normal to an element edge. In the last section, only the deflections of the control points are used as the unknowns. In this section, construction of a conforming quadrilateral element is described.

4.2.2 Normal rotations and local transformations

The proposed conforming quadrilateral element is shown in Figure 4.2 (a) with the parametric coordinates of the corner and two side nodes provided. The positions of the nodes in the global Cartesian coordinate system are determined by the geometric approximation in Equation (4.1). The element consists of four corner nodes and eight side nodes, or two side nodes for each element side. At the corner node j $(j = 1, 2, 3, 4)$, the deflection w_j and rotations θ_{xj} and θ_{yj} are considered as degrees of freedom as shown in Figure 4.2 (b). Along the element side j, the normal rotations θ_{njk}, $(k = 1, 2)$, at the two side nodes are used. Eventually, the proposed element has 20 degrees of freedom, and they are arranged in a vector of degrees of freedom $\mathbf{u}$ as

$$\mathbf{u} = \begin{matrix}[w_1 & \theta_{x1} & \theta_{y1} & \theta_{n11} & \theta_{n12} & w_2 & \theta_{x2} & \theta_{y2} & \theta_{n21} & \theta_{n22}\\ w_3 & \theta_{x3} & \theta_{y3} & \theta_{n31} & \theta_{n32} & w_4 & \theta_{x4} & \theta_{y4} & \theta_{n41} & \theta_{n42}]^{\mathrm{T}}.\end{matrix} \qquad (4.12)$$

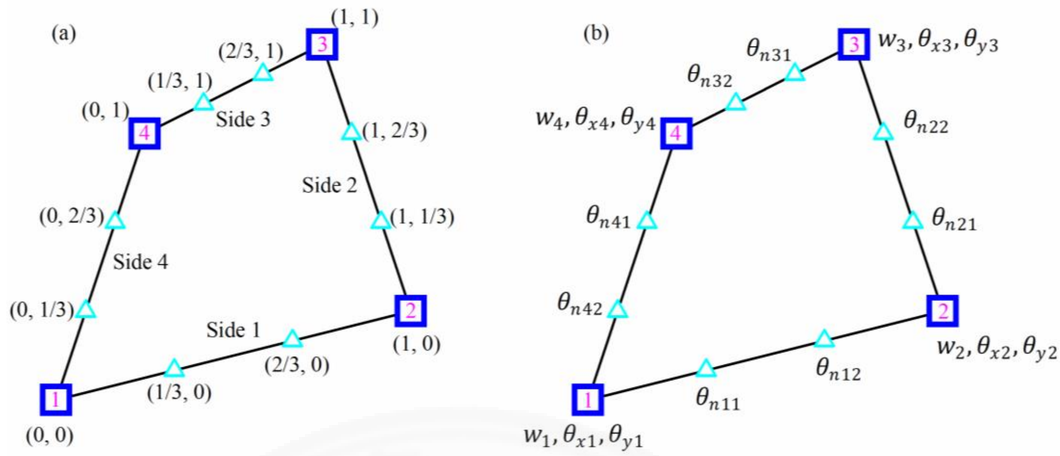

Figure 4.2 The proposed quadrilateral element. (a): Nodal parametric coordinates, (b): Nodal degrees of freedom.

Regarding the normal rotations along the element sides, the unit normal vector $\mathbf{n}$ of each side is defined in Figure 4.3. Here, n is the parametric coordinate along a vector $\mathbf{n}$. The normal rotation θ_n is defined as

$$\theta_n = \frac{\partial w}{\partial n} = n_x\theta_x + n_y\theta_y = n_x\frac{\partial w}{\partial x} + n_y\frac{\partial w}{\partial y} \tag{4.13}$$

where n_x and n_y are the components of $\mathbf{n}$ with respect to the axes $\mathbf{e}_x$ and $\mathbf{e}_y$, respectively.

In the proposed element, there are the 20 degrees of freedom as shown in Figure 4.4 (a). However, the deflection is interpolated from 16 control variables as shown in Figure 4.4 (b). Clearly, four constraints on the 20 degrees of freedom must be introduced in order that a unique transformation between the 20 degrees of freedom and the 16 control variables can be established. These four constraints are to be introduced shortly.

Consider the side 1 of the element and its associated degrees of freedom laid within the dotted frame in Figure 4.4 (a). The following relations can be written, i.e.

$$\mathbf{u}_1 = \begin{bmatrix} w_1(0,0) \\ \theta_{x1}(0,0) \\ \theta_{y1}(0,0) \\ \theta_{n11}(1/3,0) \\ \theta_{n12}(2/3,0) \\ w_2(1,0) \\ \theta_{x2}(1,0) \\ \theta_{y2}(1,0) \end{bmatrix} = \mathbf{S}_1 \begin{bmatrix} d_1 \\ d_2 \\ d_3 \\ d_4 \\ d_5 \\ d_6 \\ d_7 \\ d_8 \end{bmatrix} = \mathbf{S}_1 \mathbf{d}_1 \tag{4.14}$$

By using the approximation of w in Equation (4.2), $\mathbf{u}_1$ can be determined by $\mathbf{d}_1$, which contains the control variables laid within the dotted frame shown in Figure 4.4 (b). Consequently, the following relation is obtained, i.e.,

$$\mathbf{d}_1 = \mathbf{S}_1^{-1}\mathbf{u}_1 = \mathbf{T}_{s1}\mathbf{u}_1 \tag{4.15}$$

For the relations between the remaining control variables and degrees of freedom, the above procedure is repeated for the sides 2, 3, and 4. Eventually, three more local transformations are obtained as

$$\mathbf{d}_2 = \mathbf{T}_{s2}\mathbf{u}_2; \quad \mathbf{d}_3 = \mathbf{T}_{s3}\mathbf{u}_3; \quad \mathbf{d}_4 = \mathbf{T}_{s4}\mathbf{u}_4 \tag{4.16}$$

where the following vectors are introduced as

$$\mathbf{d}_2 = [d_3 \quad d_4 \quad d_7 \quad d_8 \quad d_{11} \quad d_{12} \quad d_{15} \quad d_{16}]^{\mathrm{T}}; \tag{4.17}$$

$$\mathbf{d}_3 = [d_9 \quad d_{10} \quad d_{11} \quad d_{12} \quad d_{13} \quad d_{14} \quad d_{15} \quad d_{16}]^{\mathrm{T}}; \tag{4.18}$$

$$\mathbf{d}_4 = [d_1 \quad d_2 \quad d_5 \quad d_6 \quad d_9 \quad d_{10} \quad d_{13} \quad d_{14}]^{\mathrm{T}}; \tag{4.19}$$

$$\mathbf{u}_2 = [w_2 \quad \theta_{x2} \quad \theta_{y2} \quad \theta_{n21} \quad \theta_{n22} \quad w_3 \quad \theta_{x3} \quad \theta_{y3}]^{\mathrm{T}}; \tag{4.20}$$

$$\mathbf{u}_3 = [w_3 \quad \theta_{x3} \quad \theta_{y3} \quad \theta_{n31} \quad \theta_{n32} \quad w_4 \quad \theta_{x4} \quad \theta_{y4}]^{\mathrm{T}}; \tag{4.21}$$

$$\mathbf{u}_4 = [w_4 \quad \theta_{x4} \quad \theta_{y4} \quad \theta_{n41} \quad \theta_{n42} \quad w_1 \quad \theta_{x1} \quad \theta_{y1}]^{\mathrm{T}}. \tag{4.22}$$

4.2.3 Unique transformation

For the derivation of the finite element equations in terms of degrees of freedom, a unique transformation between control variables and degrees of freedom is required as

$$\mathbf{d} = \mathbf{T}\mathbf{u} \tag{4.23}$$

where $\mathbf{T}$ is referred to as the transformation matrix. In the following, the construction of $\mathbf{T}$ is discussed.

It can be noticed that the local transformations of two adjacent sides involve four control variables in common. For a better discussion, the local transformations of the sides 1 and 2 are inspected. The common control variables from these sides are d_3, d_4, d_7, and d_8. The control variables d_3, d_4, and d_8 only depend on the degrees of freedom at the node 2 while the control variable d_7 are determined by different relations with the degrees of freedom on the sides 1 and 2. This phenomenon is visualized in Figure 4.5. In the figure, all the degrees of freedom are set to zero except $\theta_{x2} = 1$. The control variables d_3, d_4, d_7, and d_8 determined using the matrices $\mathbf{T}_{s1}$ and $\mathbf{T}_{s2}$ are plotted in Figure 4.5 (a)-(b), respectively. It can be observed that the control variables d_3, d_4, and d_8 are uniquely determined while two different values of d_7 are computed with a same set of degrees of freedom. This phenomenon renders the transformation in Equation (4.23) nonunique. To obtain the same values of d_7, an additional constraint is used for the degrees of freedom on the sides 1 and 2. Similarly, three more additional constraints are also employed for the control variables d_6, d_{10}, and d_{11}. These four constraints lead to the uniqueness of $\mathbf{T}$.

For the local transformations in Equations (4.15) and (4.16), components in the vectors $\mathbf{d}_j$ and $\mathbf{u}_j$ are re-arranged accordingly to their locations in the vectors $\mathbf{d}$ and $\mathbf{u}$. This re-arrangement leads to the expansion of the matrix $\mathbf{T}_{sj}$ to the matrix $\mathbf{T}_j$ with the size of 16×20. In this study, the transformation matrix $\mathbf{T}$ can be constructed as

$$\mathbf{T}(1,:) = \mathbf{T}_1(1,:) \qquad \mathbf{T}(2,:) = \mathbf{T}_1(2,:) \tag{4.24}$$

$$\mathbf{T}(3,:) = \mathbf{T}_1(3,:) \qquad \mathbf{T}(4,:) = \mathbf{T}_1(4,:) \tag{4.25}$$

$$\mathbf{T}(5,:) = \mathbf{T}_4(5,:) \qquad \mathbf{T}(6,:) = 0.5[\mathbf{T}_1(6,:) + \mathbf{T}_4(6,:)] \tag{4.26}$$

$$\mathbf{T}(7,:) = 0.5[\mathbf{T}_1(7,:) + \mathbf{T}_2(7,:)] \qquad \mathbf{T}(8,:) = \mathbf{T}_2(8,:) \tag{4.27}$$

$$\mathbf{T}(9,:) = \mathbf{T}_4(9,:) \qquad \mathbf{T}(10,:) = 0.5[\mathbf{T}_3(10,:) + \mathbf{T}_4(10,:)] \tag{4.28}$$

$$\mathbf{T}(11,:) = 0.5[\mathbf{T}_2(11,:) + \mathbf{T}_3(11,:)] \qquad \mathbf{T}(12,:) = \mathbf{T}_2(12,:) \tag{4.29}$$

$$\mathbf{T}(13,:) = \mathbf{T}_4(13,:) \qquad \mathbf{T}(14,:) = \mathbf{T}_4(14,:) \tag{4.30}$$

$$\mathbf{T}(15,:) = \mathbf{T}_3(15,:) \qquad \mathbf{T}(16,:) = \mathbf{T}_3(16,:). \tag{4.31}$$

Regarding the additional constraints of the degrees of freedom, a matrix **L** is constructed as

$$\mathbf{L}(1,:) = \mathbf{T}_1(6,:) - \mathbf{T}_4(6,:) \qquad \mathbf{L}(2,:) = \mathbf{T}_1(7,:) - \mathbf{T}_2(7,:) \tag{4.32}$$

$$\mathbf{L}(3,:) = \mathbf{T}_3(10,:) - \mathbf{T}_4(10,:) \qquad \mathbf{L}(4,:) = \mathbf{T}_2(11,:) - \mathbf{T}_3(11,:). \tag{4.33}$$

In Equations (4.23)-(4.33), $\mathbf{T}(l,:)$, $\mathbf{T}_j(l,:)$, and $\mathbf{L}(l,:)$ represent the l-th row of the matrices $\mathbf{T}$, $\mathbf{T}_j$, and **L**, respectively. The four constraints are set as follows:

$$[d_6 \text{ from side 1}] - [d_6 \text{ from side 4}] = \mathbf{L}(1,:)\mathbf{u} = 0; \tag{4.34}$$

$$[d_7 \text{ from side 1}] - [d_7 \text{ from side 2}] = \mathbf{L}(2,:)\mathbf{u} = 0; \tag{4.35}$$

$$[d_{10} \text{ from side 3}] - [d_{10} \text{ from side 4}] = \mathbf{L}(3,:)\mathbf{u} = 0; \tag{4.36}$$

$$[d_{11} \text{ from side 2}] - [d_{11} \text{ from side 3}] = \mathbf{L}(4,:)\mathbf{u} = 0 \tag{4.37}$$

which yields

$$\mathbf{Lu} = \mathbf{0}. \tag{4.38}$$

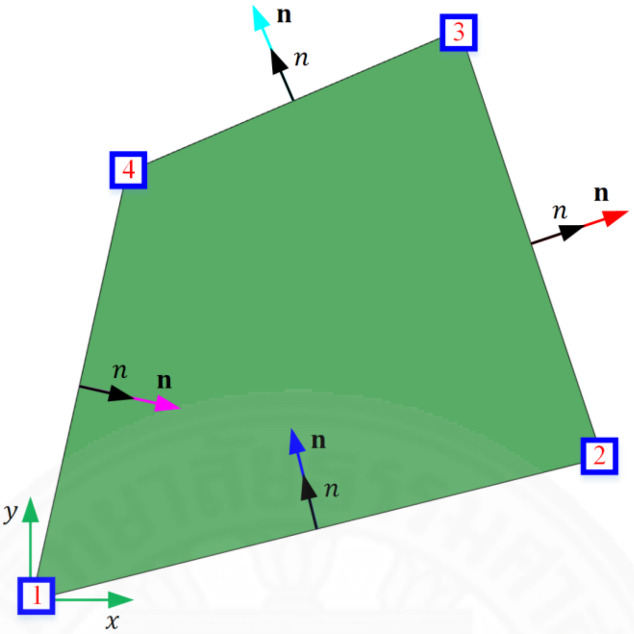

Figure 4.3 Normal rotations.

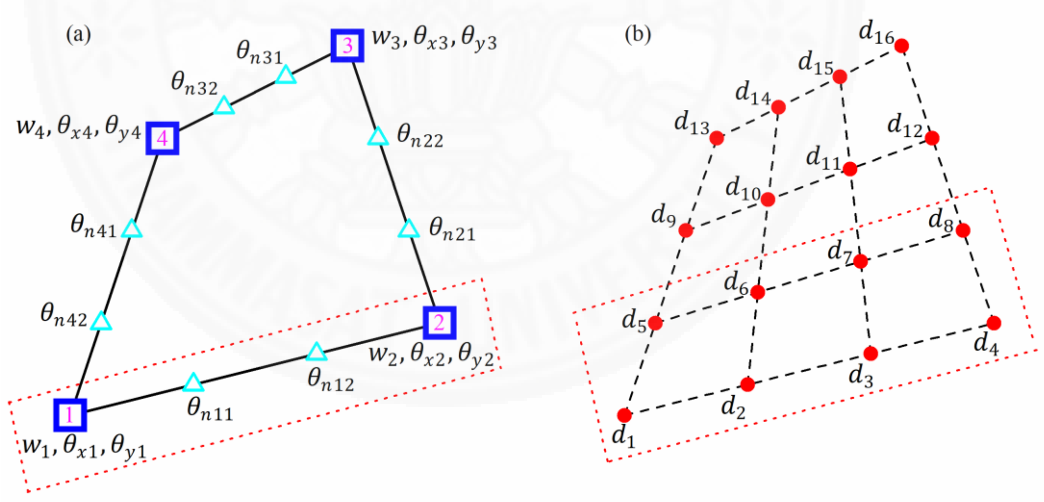

Figure 4.4 The proposed quadrilateral element – Local transformations. (a): Degrees of freedom, (b): Control variables.

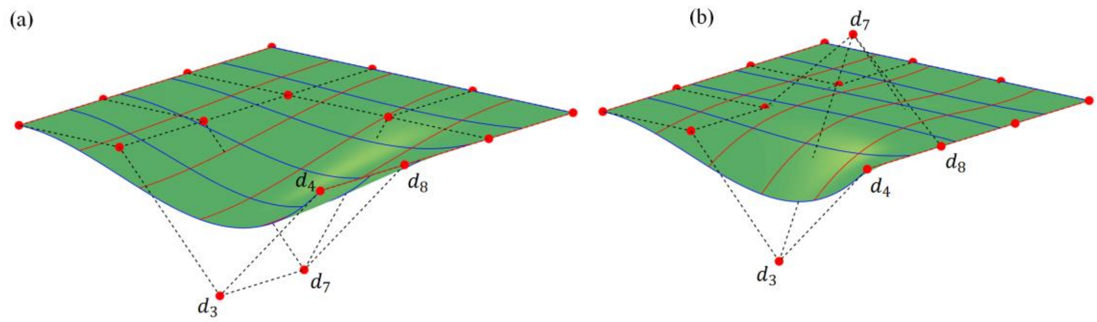

Figure 4.5 The proposed quadrilateral element – Affected control variables and degrees of freedom of element sides. (a): side 1, (b): side 2.

4.3 The constrained finite element formulation

The penalty method is used to incorporate Equation (4.38) into the finite element formulation. One of the advantages of the penalty method is that it does not increase the number of unknowns per element. Note that the accuracy of this approach depends on the penalty coefficient. Denote the penalty coefficient by α. Define the total potential energy as

$$\Pi = U + \bar{V} + \frac{1}{2}\alpha(\mathbf{Lu})^{\mathrm{T}}\mathbf{Lu} \tag{4.39}$$

where U is the strain energy and $\bar{V}$ is the potential energy of the applied loads. By referring to Equations (4.2), (4.5), and (4.6), they are defined as

$$U = \frac{1}{2}\int_V \boldsymbol{\varepsilon}^{\mathrm{T}}\boldsymbol{\sigma}\, dV = \frac{1}{2}\mathbf{d}^{\mathrm{T}}\mathbf{Kd}; \tag{4.40}$$

$$\bar{V} = -\mathbf{d}^{\mathrm{T}}\mathbf{F}. \tag{4.41}$$

Equation (4.39) is rewritten as

$$\Pi = \frac{1}{2}\mathbf{d}^{\mathrm{T}}\mathbf{Kd} - \mathbf{d}^{\mathrm{T}}\mathbf{F} + \frac{1}{2}\alpha(\mathbf{Lu})^{\mathrm{T}}\mathbf{Lu}. \tag{4.42}$$

Substituting Equation (4.23) into Equation (4.42) yields

$$\Pi = \frac{1}{2}(\mathbf{Tu})^{\mathrm{T}}\mathbf{KTu} - (\mathbf{Tu})^{\mathrm{T}}\mathbf{F} + \frac{1}{2}\alpha(\mathbf{Lu})^{\mathrm{T}}\mathbf{Lu}; \tag{4.43}$$

The variation of Equation (4.43) is expressed as

$$\delta\Pi = \frac{1}{2}\delta(\mathbf{Tu})^{\mathrm{T}}\mathbf{KTu} + \frac{1}{2}(\mathbf{Tu})^{\mathrm{T}}\mathbf{KT}\delta\mathbf{u} - \delta(\mathbf{Tu})^{\mathrm{T}}\mathbf{F} + \frac{1}{2}\alpha\delta(\mathbf{Lu})^{\mathrm{T}}\mathbf{Lu} + \frac{1}{2}\alpha(\mathbf{Lu})^{\mathrm{T}}\mathbf{L}\delta\mathbf{u}; \tag{4.44}$$

$$\delta\Pi = \delta\mathbf{u}^{\mathrm{T}}\mathbf{T}^{\mathrm{T}}\mathbf{KTu} - \delta\mathbf{u}^{\mathrm{T}}\mathbf{T}^{\mathrm{T}}\mathbf{F} + \delta\mathbf{u}^{\mathrm{T}}(\mathbf{L}^{\mathrm{T}}\alpha\mathbf{Lu}); \tag{4.45}$$

$$\delta\Pi = \delta\mathbf{u}^{\mathrm{T}}(\mathbf{T}^{\mathrm{T}}\mathbf{KTu} - \mathbf{T}^{\mathrm{T}}\mathbf{F} + \mathbf{L}^{\mathrm{T}}\alpha\mathbf{Lu}). \tag{4.46}$$

In order to minimize Π, it follows that

$$\delta\Pi = \delta\mathbf{u}^{\mathrm{T}}(\mathbf{T}^{\mathrm{T}}\mathbf{KTu} - \mathbf{T}^{\mathrm{T}}\mathbf{F} + \mathbf{L}^{\mathrm{T}}\alpha\mathbf{Lu}) = 0. \tag{4.47}$$

Since $\delta\mathbf{u}^{\mathrm{T}}$ is arbitrary, the compact form of the constrained finite element equation is obtained as

$$(\mathbf{T}^{\mathrm{T}}\mathbf{KT} + \mathbf{L}^{\mathrm{T}}\alpha\mathbf{L})\mathbf{u} = \mathbf{T}^{\mathrm{T}}\mathbf{F}. \tag{4.48}$$

It is worth noting the penalty coefficient α does affect the accuracy of this proposed method. For convenience, the penalty coefficient α is expressed in terms of the geometrical and material properties of the plate as (Greco, Cuomo & Contrafatto, 2019)

$$\alpha = k\frac{Eh^3}{12(1-\nu^2)}(1-\nu) = kD(1-\nu) \tag{4.49}$$

where k is referred to as the penalty parameter and D is defined as

$$D = \frac{Eh^3}{12(1-\nu^2)}.$$

CHAPTER 5
NUMERICAL EXAMPLES

In this chapter, some well-established problems, e.g., the bending patch test, square plate with unstructured mesh, circular plate, and square cutout plate are examined. The aim is to investigate the robustness, efficiency of this proposed quadrilateral conforming element. In this study, for all considered examples, the material properties and the plate thickness are set as follows: $E = 10^8$, $\nu = 0.25$, $h = 10^{-3}$.

5.1 Patch test with a constant bending moment

This example is concerned the bending of a square plate with unit length, i.e., $L = 1$. Loading and boundary conditions are shown in Figure 5.1 (a). The plate is simply supported and subjected to a pair of opposite bending moments on the left and right sides, whereas the normal rotations along the bottom and top sides are zero. The exact solution for the deflection of the plate is available in the work by Greco, Cuomo and Contrafatto (2019) as

$$w_{ex} = \frac{M_x x}{2D}(L - x) \tag{5.1}$$

The plate is analyzed using four elements with distortion meshes characterized by a parameter a. To test the accuracy and robustness of the proposed element with distortions, three meshes with three values of a are considered, i.e., $a = 0$, 0.2, and 0.4. The mesh with $a = 0.4$ is shown in Figure 5.1 (b).

First, to verify the accuracy of the proposed element, the numerical results for the deflection obtained from the three meshes are plotted in Figure 5.2 (a). It is noted here that $k = 10^7$ is used for the analysis. Excellent agreement between the numerical results and exact solution is observed. One should note the severe distortion of the elements shown in Figure 5.2 (b) when $a = 0.4$. From the obtained results, the accuracy and robustness of the proposed element, when used with distorted meshes, are validated. The deformation of the plate is visualized in Figure 5.2 (b), and the conformity between elements is perfectly shown.

In general, the accuracy of the penalty method depends on the values of the penalty coefficient α, or the penalty parameter k in this study. They are problem-dependent and not known a priori. Therefore, the effect of different choices of k should be inspected to determine a range of values, which can be used in practice. Figure 5.3 shows the ratio between the numerical results and the exact solution of the center deflection, i.e., $w(0.5, 0.5)/w_{ex}(0.5, 0.5)$. It is found that there is a very wide range of the value of k in which the exact solution is virtually produced, i.e., from 10^4 to 10^{14}.

Furthermore, this experiment also indicates that using small values of k, e.g., smaller than 10^4 in this example, provides inaccurate results due to the weak enforcements of the constraints between the degrees of freedom. For the high values of k, e.g., higher than 10^{14} in this example, the penalty method leads to ill-conditioning problems, and inaccurate results are inevitably obtained. In this study, k is set to be 10^7 for all the analysis. The accuracy of this choice has been confirmed in this example and is further confirmed in subsequent examples.

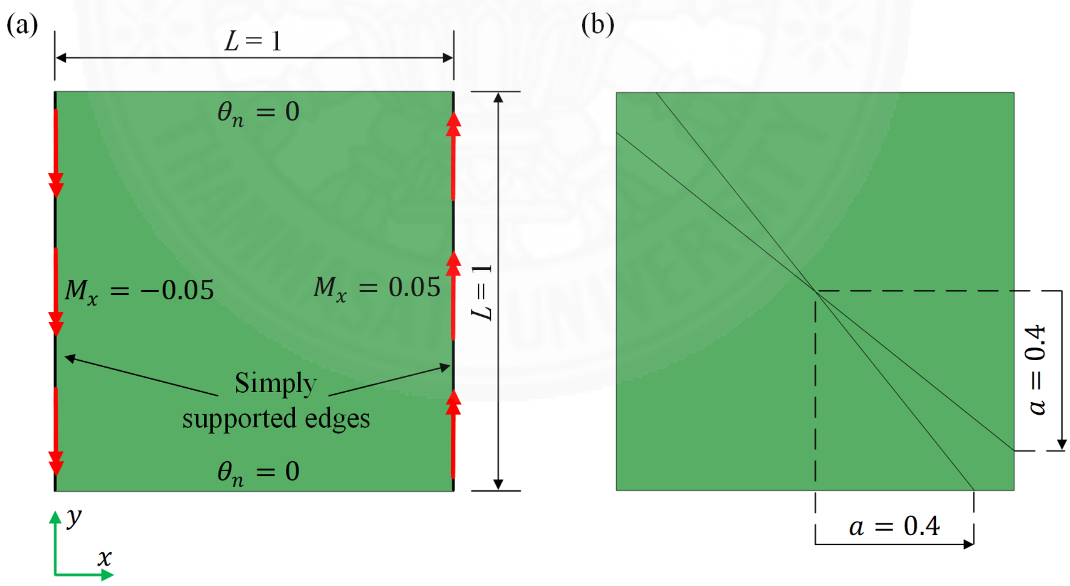

Figure 5.1 A square simply supported plate with a constant bending moment. (a): Loading and boundary conditions, (b): Mesh definition.

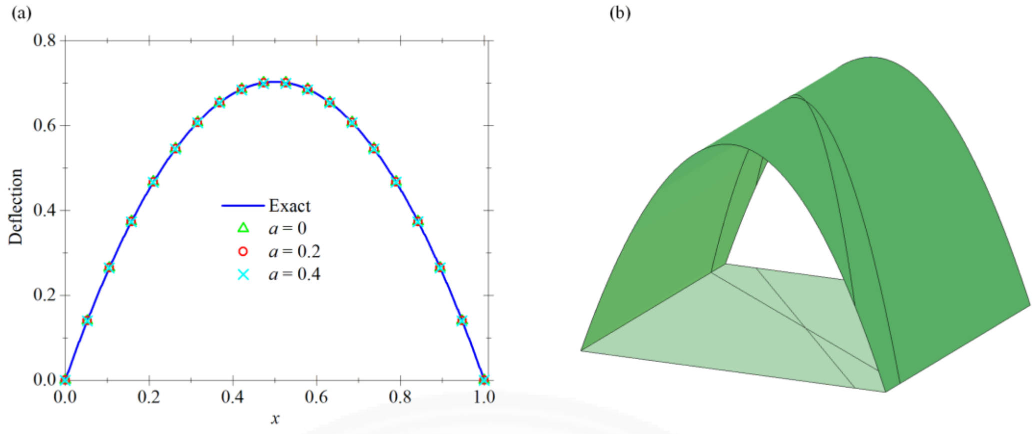

Figure 5.2 A square simply supported plate with a constant bending moment. (a): Deflections of three meshes, (b): Deformation of the plate.

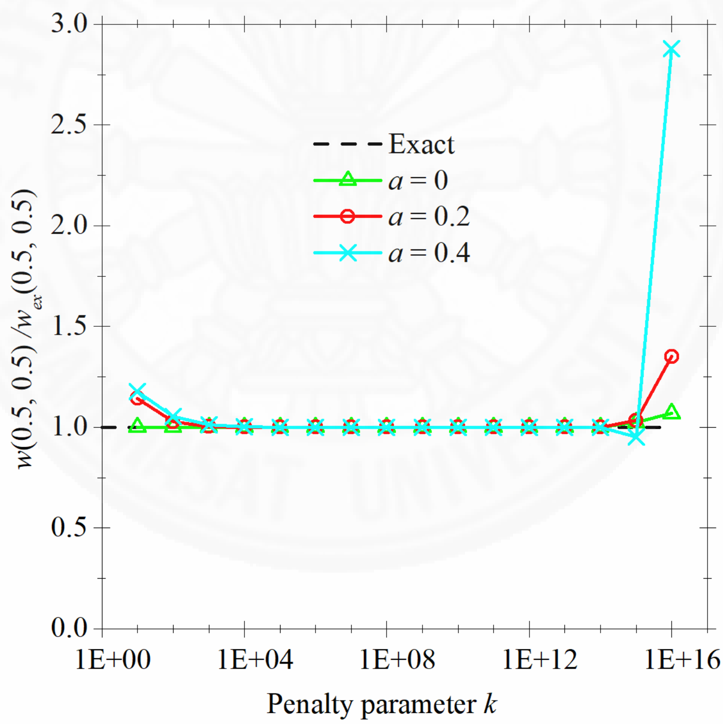

Figure 5.3 A square simply supported plate with a constant bending moment – influence of the penalty parameter to the deflection at the center.

5.2 A Simply supported square plate

In this example, a simply supported square plate of unit length, i.e., $L = 1$, shown in Figure 5.4 is considered. The plate is subjected to a uniformly distributed force $f_z = 1.5$. With the given loading and boundary conditions, the exact solution for the deflection of the plate can be derived as

$$w_{ex}(x, y) = \frac{16 f_z}{\pi^6 D} \sum_{m=1,3}^{\infty} \sum_{n=1,3}^{\infty} \frac{\sin\left(\frac{m\pi x}{L}\right) \sin\left(\frac{n\pi y}{L}\right)}{mn\left(\frac{m^2 + n^2}{L^2}\right)^2}. \tag{5.2}$$

The plate is analyzed using three unstructured meshes shown in Figure 5.5 (a)-(c). The mesh distortion is characterized by a parameter a. For each unstructured mesh, three values of a are considered, i.e., $a = L/16$, $L/8$, and $L/4$.

The deflection of the plate along the line $y = L/2$, i.e., $w(x, L/2)$, obtained using the three meshes with 8×8 elements for the value of $a = L/4$ are plotted in Figure 5.6. Excellent agreement between the numerical results and the exact solution is found. Furthermore, the deformations of the plate from the three meshes are visualized in Figure 5.7. The continuity of slopes across elements is perfectly depicted.

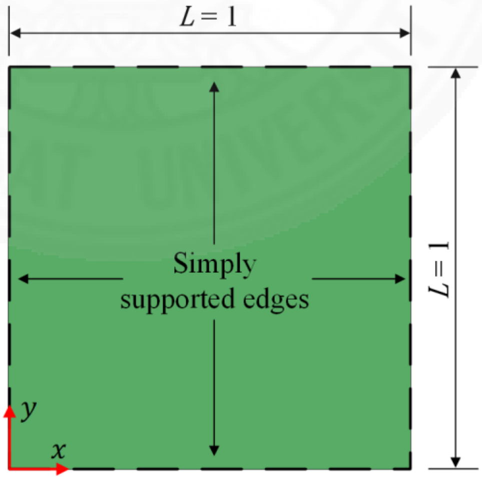

Figure 5.4 A simply supported square plate – Problem set up.

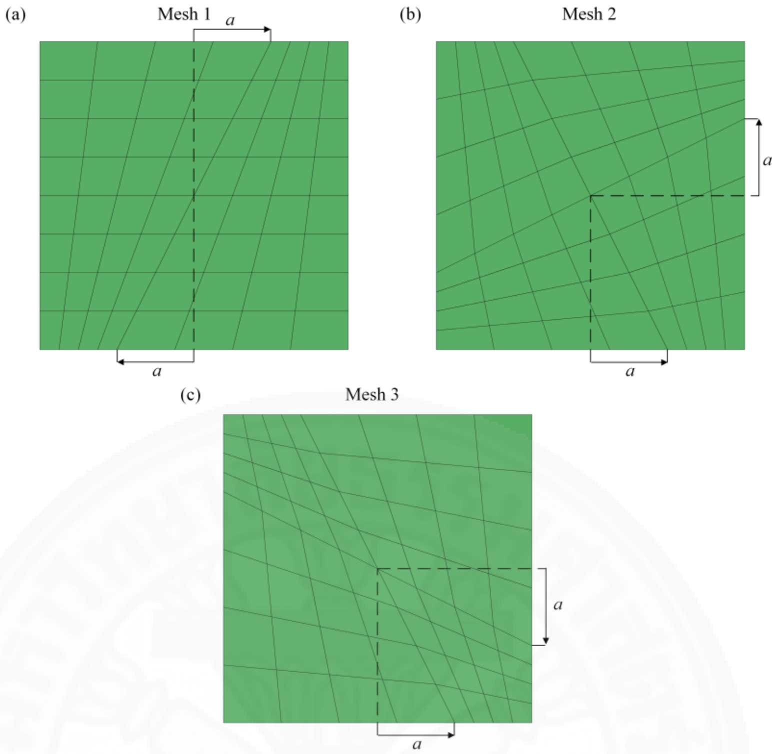

Figure 5.5 A simply supported square plate – Unstructured meshes. (a): Mesh 1, (b): Mesh 2, (c): Mesh 3.

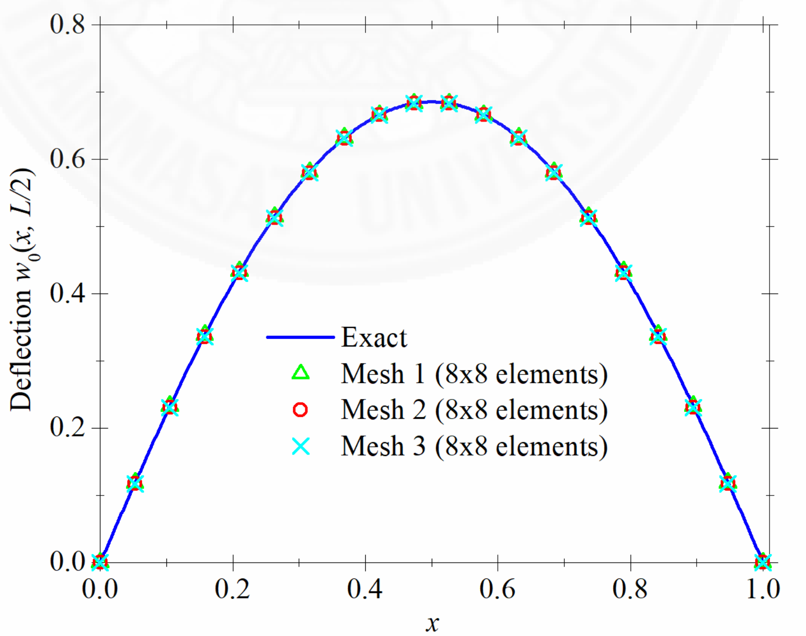

Figure 5.6 A simply supported square plate – Deformations with 8×8 elements for $a = L/4$. (a): Mesh 1, (b): Mesh 2, (c): Mesh 3.

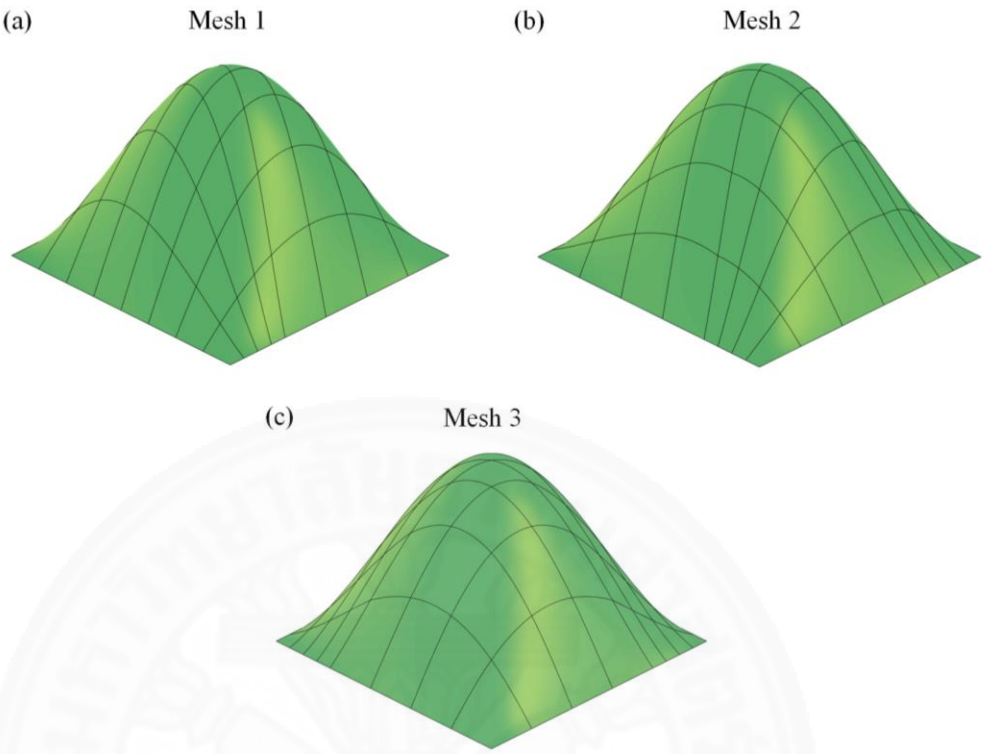

Figure 5.7 A simply supported square plate – Deformations with 8×8 elements for $a = L/4$. (a): Mesh 1, (b): Mesh 2, (c): Mesh 3.

In this example, the convergence test is performed for relative errors of the strain energy. The exact solution for the strain energy is given by

$$U_{ex} = \frac{32(f_z)^2 L^6}{\pi^8 D} \sum_{m=1,3}^{\infty} \sum_{n=1,3}^{\infty} \frac{1}{m^2 n^2 (m^2 + n^2)^2}. \tag{5.3}$$

The numerical strain energy is denoted by U_{num}. Results are shown in Figure 5.8. It is recalled that the optimal order of convergence is 4. It can be observed that the optimal order of convergence is achieved for all the meshes considered. On the other hand, results obtained from the meshes 1 and 2 can be considered insensitive with the distortion of elements since the difference in the accuracy is neglectable. The effect of distortion of elements on the mesh 3 is noticeable when a slight loss of accuracy if found with $a = L/4$. In addition, Table 5.1, Table 5.2, and Table 5.3 report the numerical results and the percentage error in terms of strain energy for all three considered meshes.

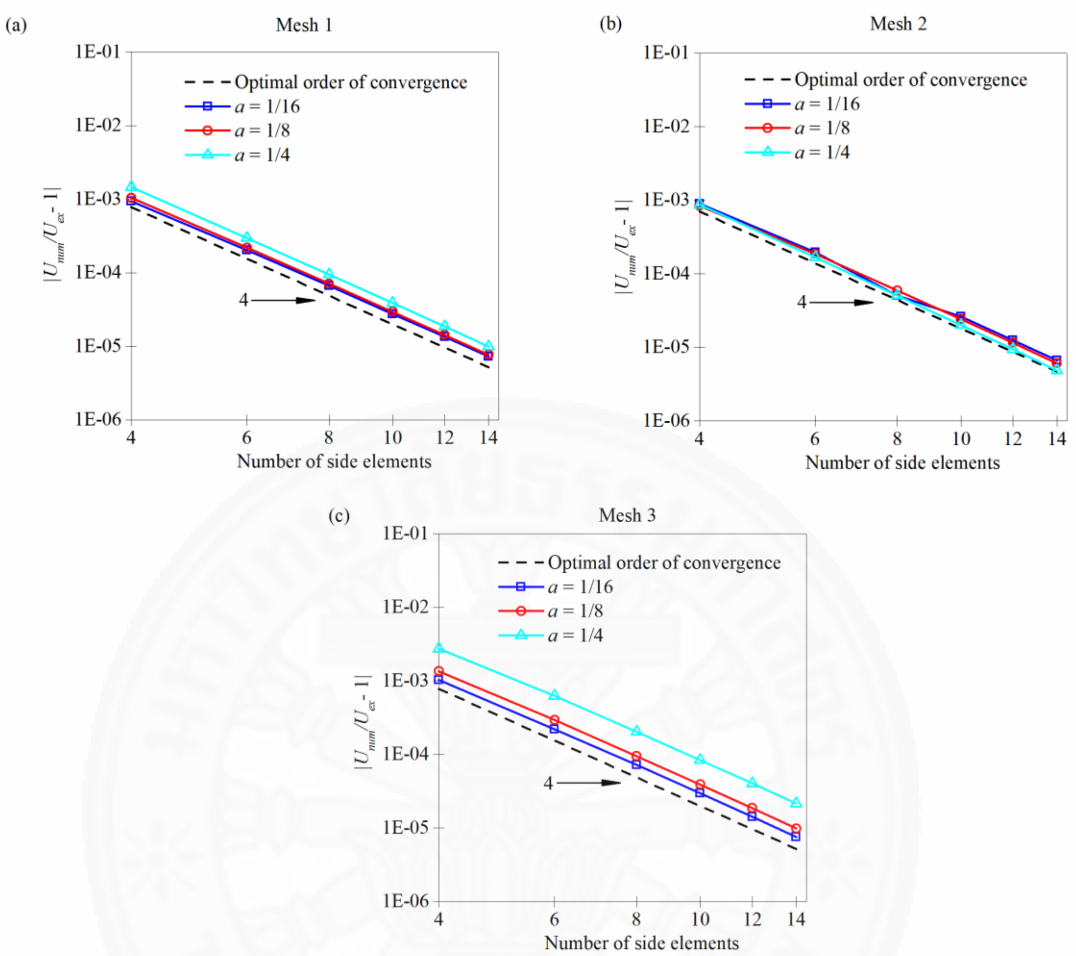

Figure 5.8 A simply supported square plate – Convergence test for the strain energy. (a): Mesh 1, (b): Mesh 2, (c): Mesh 3.

Table 5.1 Simply supported square plate (Mesh 1).

N_{se}	N_{dofs}	Mesh 1					
		$a = L/16$		$a = L/8$		$a = L/4$	
		U_{num}	$\mathcal{P}$	U_{num}	$\mathcal{P}$	U_{num}	$\mathcal{P}$
4	155	0.215270	0.09433	0.215250	0.10378	0.215159	0.14586
6	315	0.215430	0.02026	0.215426	0.02190	0.215410	0.02960
8	531	0.215459	0.00662	0.215458	0.00711	0.215453	0.00945
10	803	0.215468	0.00275	0.215467	0.00295	0.215465	0.00389
12	1131	0.215471	0.00134	0.215470	0.00143	0.215469	0.00188

14	1515	0.215472	0.00072	0.215472	0.00077	0.215471	0.00101
$U_{ex} = 0.215473$							

Note $\mathcal{P} = (|U_{num}/U_{ex} - 1|) \times 100\%$.

Table 5.2 Simply supported square plate (Mesh 2).

N_{se}	N_{dofs}	Mesh 1					
		$a = L/16$		$a = L/8$		$a = L/4$	
		U_{num}	$\mathcal{P}$	U_{num}	$\mathcal{P}$	U_{num}	$\mathcal{P}$
4	155	0.215282	0.08903	0.215293	0.08387	0.215287	0.08698
6	315	0.215432	0.01951	0.215434	0.01866	0.215438	0.01678
8	531	0.215460	0.00633	0.215461	0.00592	0.215463	0.00507
10	803	0.215468	0.00263	0.215469	0.00244	0.215470	0.00202
12	1131	0.215471	0.00128	0.215471	0.00118	0.215472	0.00094
14	1515	0.215472	0.00069	0.215473	0.00064	0.215473	0.00050
$U_{ex} = 0.215473$							

Table 5.3 Simply supported square plate (Mesh 3).

N_{se}	N_{dofs}	Mesh 1					
		$a = L/16$		$a = L/8$		$a = L/4$	
		U_{num}	$\mathcal{P}$	U_{num}	$\mathcal{P}$	U_{num}	$\mathcal{P}$
4	155	0.215253	0.10240	0.215183	0.13512	0.214885	0.27325
6	315	0.215426	0.02213	0.215411	0.02938	0.215339	0.06254
8	531	0.215458	0.00723	0.215453	0.00951	0.215430	0.02036
10	803	0.215468	0.00300	0.215466	0.00393	0.215456	0.00843
12	1131	0.215471	0.00145	0.215470	0.00190	0.215465	0.00407
14	1515	0.215472	0.00079	0.215472	0.00102	0.215469	0.00219
$U_{ex} = 0.215473$							

5.3 A clamped circular plate

In this example, a clamped circular plate is considered, and many advantages of using the proposed element are illustrated. As shown in Figure 5.9, the plate is clamped along the edge and subjected to a uniformly distributed force $f_z = 2.5$. The radius of the plate is $R = 0.5$. The exact solution for the deflection of the plate is available in Timoshenko and Woinowsky-Krieger (1959) as

$$w_{ex}(r) = \frac{f_Z(r^2 - R^2)^2}{64D} \tag{5.4}$$

where r is the radial coordinate.

Here, the advantages of using the proposed element for geometric approximations of plates with curved boundaries are illustrated. Figure 5.9 shows three meshes, i.e., 2×2, 4×4, and 8×8 elements. It can be observed that the plate is exactly represented even with the very coarse mesh of 2×2 elements. A comparison between the numerical results obtained by the three meshes and the exact solution of the deflection is shown in Figure 5.10 (a). Except for the coarse mesh of 2×2 elements, the accurate results are produced using the meshes of 4×4 and 8×8 elements. Additionally, the conformity between elements is confirmed by the deformation of the plate with the mesh of 4×4 elements in Figure 5.10 (b). The continuity of the rotations, or slopes, across the elements is observed.

The plate is also analyzed in Marc-Mentat, a commercial finite element package, using the popular non-conforming four-noded quadrilateral elements. The convergence test is shown in Figure 5.11 (a) using the relative errors of the center deflection computed by using Marc-Mentat and the proposed element. One can observe that the proposed element provides higher accuracy and order of convergence. In fact, the convergence property is one of the most prominent features of using conforming plate elements. To clarify this statement, the relative errors of the center deflection are plotted as functions of the number of side elements in Figure 5.11 (b). As indicated in the work by Greco, Cuomo and Contrafatto (2019), the optimal order of convergence is 4. In this example, the optimal order of convergence is achieved by using the proposed element while Marc-Mentat offers only a quadratic order of convergence. In addition, the numerical results and percentage errors in terms of the maximum deflection are reported in Table 5.4.

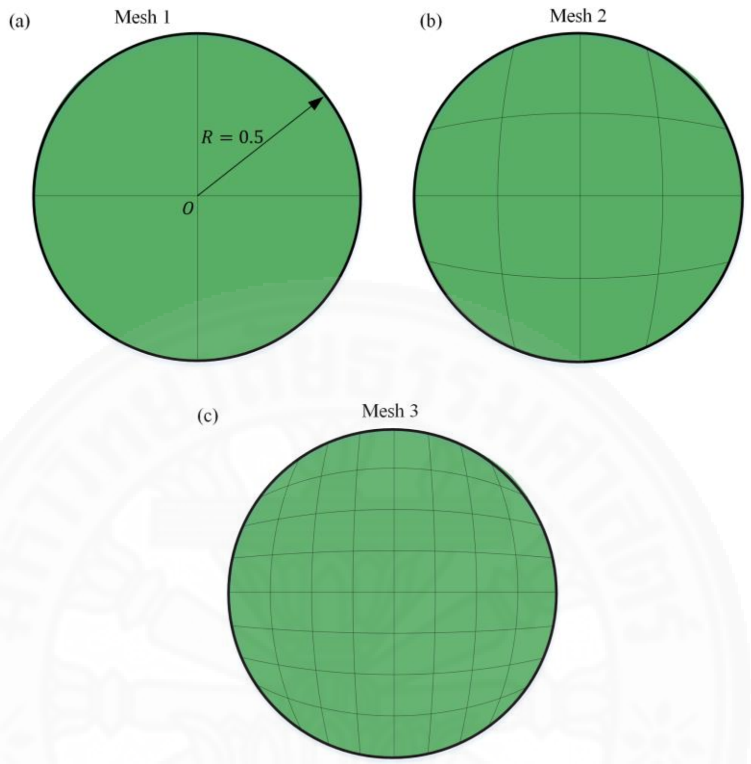

Figure 5.9 A clamped circular plate – Meshes of elements. (a): Mesh 1, (b): Mesh 2, (c): Mesh 3.

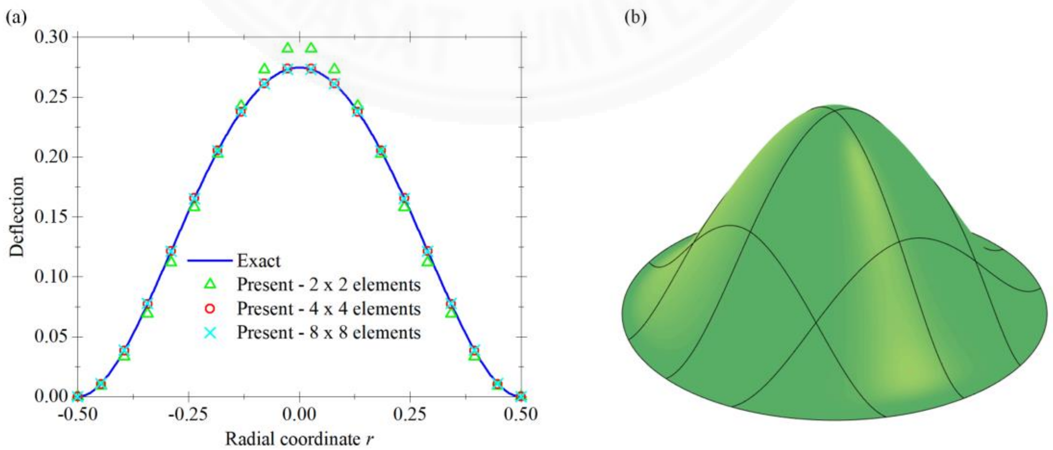

Figure 5.10 A clamped circular plate. (a): Deflection, (b): Deformation of the plate with the mesh of 4×4 elements.

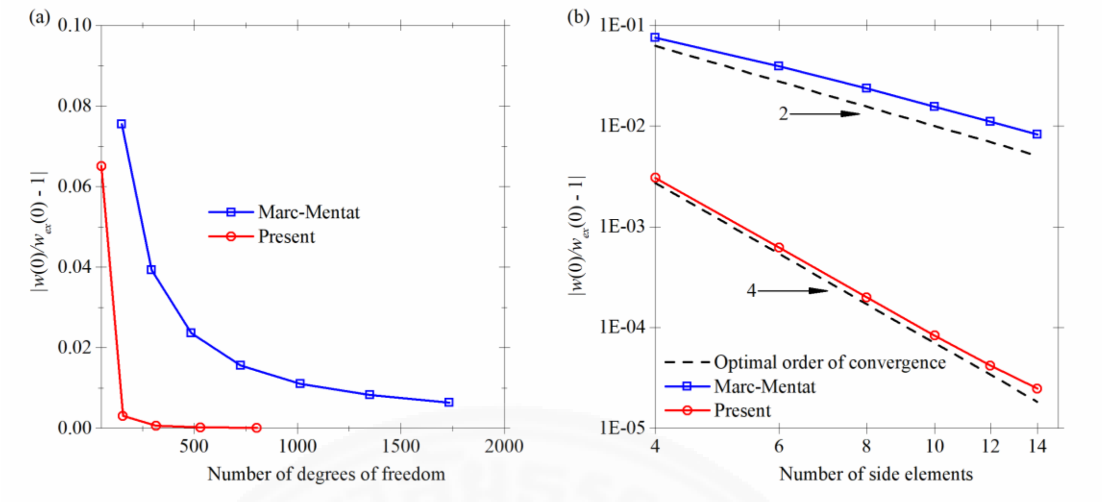

Figure 5.11 A clamped circular plate. (a): Comparison of the convergence properties between the proposed element and Marc-Mentat, (b): Order of convergence for the relative errors of the center deflection versus the number of side elements.

Table 5.4 The numerical results and percentage errors of the central deflection of the circular plate.

Marc-Mentat				Present study			
N_{se}	N_{dofs}	$w(0)$	$\mathcal{P}$	N_{se}	N_{dofs}	$w(0)$	$\mathcal{P}$
4	150	0.29539	7.54749	2	51	0.29253	6.50746
6	294	0.28545	3.92917	4	155	0.27550	0.30713
8	384	0.28115	2.36432	6	315	0.27483	0.06226
10	600	0.27895	1.56332	8	531	0.27471	0.01992
12	1014	0.27770	1.10676	10	803	0.27468	0.00831
14	1350	0.27692	0.82386	12	1131	0.27467	0.00419
16	1734	0.27641	0.63599	14	1515	0.27467	0.00248
$w_{ex}(0) = 0.27465$							

Note $\mathcal{P} = (|w(0)/w_{ex}(0) - 1|) \times 100\%$.

5.4 Clamped cutout square plate

The last example is to examine a square plate with a complex cutout in order to illustrate the capacity of the proposed element for the analysis of plates with complicated geometry. Figure 5.12 (a) shows the geometry and boundary conditions of the plate. The plate is fully clamped at the inner and outer edges. A uniformly distributed force $f_z = 1$ is applied. Due to the symmetry, it is enough to analyze only a quarter of the plate as shown in Figure 5.12 (b). It can be observed that the geometry of the quarter is exactly represented by using only two proposed elements.

Figure 5.13 (a)-(b) show the contour plots for the deflection of the plate obtained by using Marc-Mentat and the proposed element, respectively. The non-conforming four-noded quadrilateral elements in Marc-Mentat are used for result comparison. Very good agreement between the two contour plots is found. Moreover, the maximum deflection of the plate is also reported in Table 5.5. A significantly higher number of degrees of freedom from Marc-Mentat is used to achieve the same accuracy of using the proposed element.

The deformation of the plate is shown in Figure 5.14 with a mesh of 4×4 proposed elements. The conformity between elements is observed.

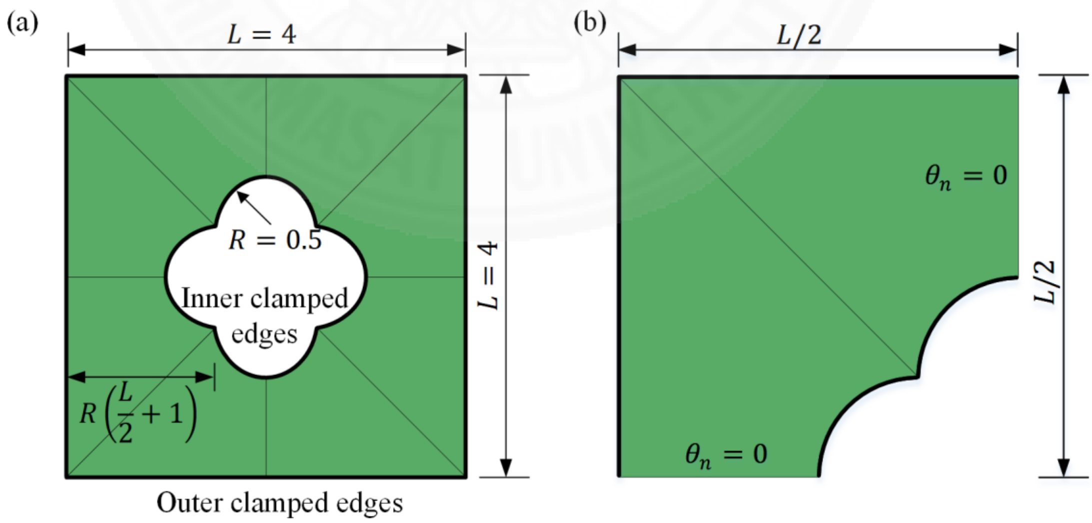

Figure 5.12 A clamped cutout square plate. (a): Problem set up, (b): Equivalent model.

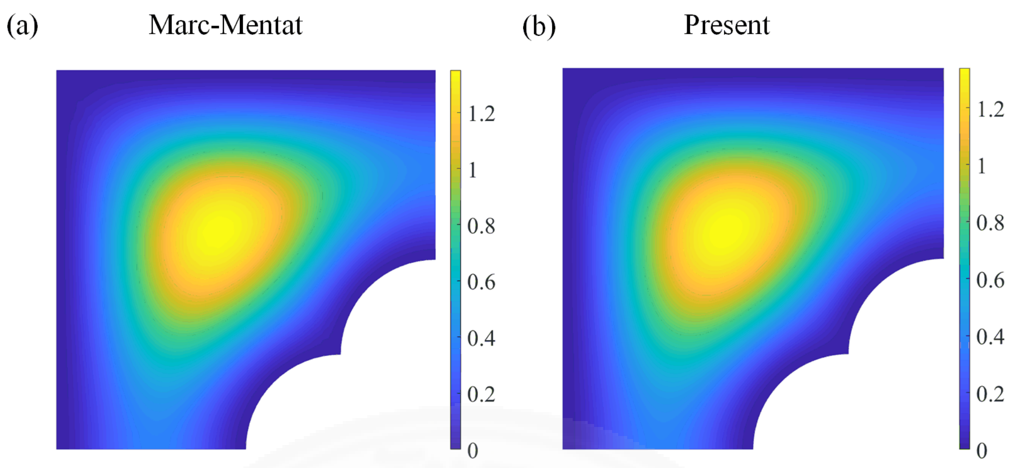

Figure 5.13 A clamped cutout square plate – Contour plot for the deflection. (a): Marc-Mentat, (b): Present.

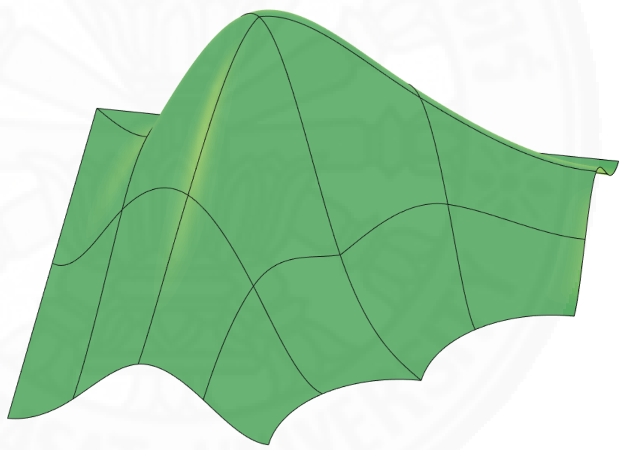

Figure 5.14 A clamped cutout plate – Deformation with a mesh of 4 × 4 proposed element.

Table 5.5 Numerical results for cutout square plate.

Marc-Mentat			Present study		
N_{se}	N_{dofs}	Maximum deflection	N_{se}	N_{dofs}	Maximum deflection
8	486	1.444	4	155	1.067
16	1734	1.383	6	315	1.296
32	6534	1.385	8	531	1.324
64	25350	1.342	10	803	1.337
128	99846	1.341	12	1131	1.339
256	363948	1.340	14	1515	1.339

CHAPTER 6
CONCLUSIONS

In this study, a new quadrilateral conforming Kirchhoff plate element is presented. The finite element formulation is straightforwardly formulated in a Cartesian coordinate system. Both geometry and the displacement field are approximated rational Bézier basis functions. The continuity between elements is enforced by considering the transverse displacement, the two rotational displacements at the corner nodes, and the rotations around element edges as the degrees of freedom. The number of control variables used in the Bézier surface for the approximation of the displacement and the number of final degrees of freedom are not the same. As a result, a unique transformation between the control variables and the final degrees of freedom is derived by introducing some additional constraints between the degrees of freedom. These constraints are handled by using the penalty method. Although the accuracy of the penalty method depends on the choice of a problem-dependent parameter, there exists a very wide range of the penalty parameter value in which accurate results are obtained.

The main advantages of the proposed quadrilateral conforming plate element are summarized as follows:

- The geometry of plates with curved edges can be represented effectively by using rational Bézier surfaces;
- The continuity of the displacement and rotations across elements can be ensured with the use of the transverse displacement, the rotational displacements at the corner nodes, and the rotations about the element edges as the degrees of freedom;
- This proposed element passes the bending patch test.

Some benchmark problems, e.g., the bending patch test, several unstructured meshes with highly distorted elements, and plates with curved boundaries (i.e., circular plate and cutout plate), are used to test the robustness and the accuracy of the proposed plate element. The rates of convergence are found to be satisfactory. The numerical results present excellent agreement with those results in the literature and from a commercial finite element program. With these features, the accuracy and efficiency of this new quadrilateral element are fully validated.

REFERENCES

Benson, D. J., Bazilevs, Y., Hsu, M. C., & Hughes, T. J. R. (2010). Isogeometric shell analysis: The Reissner–Mindlin shell. *Computer Methods in Applied Mechanics and Engineering*, *199*(5), 276-289.

Bogner, F. K., Fox, R. L., & Schmit, L. A. (1965). The generation of interelement-compatible stiffness and mass matrices by the use of interpolation formulas. *Proceeding of Proc. Conf. Matrix Meth. Struct. Mech.* (pp. 397-443). Wright Patterson Air Force Base.

Clough, R. W., & Felippa, C. A. (1968). A refined quadrilateral element for analysis of plate bending. *Proceeding of Proc. 2nd Conf. on Matrix Methods in Structural Mechanics* (pp. 43). CALIFORNIA UNIV BERKELEY.

Cottrell, J., Hughes, T., & Reali, A. (2007). Studies of refinement and continuity in isogeometric structural analysis. *Computer Methods in Applied Mechanics and Engineering*, *196*(41-44), 4160-4183.

Cottrell, J. A., Hughes, T. J. R., & Reali, A. (2007). Studies of refinement and continuity in isogeometric structural analysis. *Computer Methods in Applied Mechanics and Engineering*, *196*(41), 4160-4183.

Cuomo, M., & Greco, L. (2018). An implicit strong G1-conforming formulation for the analysis of the Kirchhoff plate model. *Continuum Mechanics and Thermodynamics*, 1-25. https://doi.org/10.1007/s00161-018-0701-3

De Luycker, E., Benson, D. J., Belytschko, T., Bazilevs, Y., & Hsu, M. C. (2011). X-FEM in isogeometric analysis for linear fracture mechanics. *International Journal for Numerical Methods in Engineering*, *87*(6), 541-565.

Fischer, P., Klassen, M., Mergheim, J., Steinmann, P., & Müller, R. (2011). Isogeometric analysis of 2D gradient elasticity. *Computational Mechanics*, *47*(3), 325-334.

Greco, L., Cuomo, M., & Contrafatto, L. (2019). A quadrilateral G1-conforming finite element for the Kirchhoff plate model. *Computer Methods in Applied Mechanics and Engineering*, *346*, 913-951.

Greco, L., Cuomo, M., & Contrafatto, L. (2019). Two new triangular G1-conforming finite elements with cubic edge rotation for the analysis of Kirchhoff plates. *Computer Methods in Applied Mechanics and Engineering*, *356*, 354-386. https://doi.org/10.1016/j.cma.2019.07.026

Hassani, B., Tavakkoli, S. M., & Moghadam, N. Z. (2011). Application of isogeometric analysis in structural shape optimization. *Scientia Iranica*, *18*(4), 846-852.

Hughes, T. J. R., Cottrell, J. A., & Bazilevs, Y. (2005). Isogeometric analysis: CAD, finite elements, NURBS, exact geometry and mesh refinement. *Computer Methods in Applied Mechanics and Engineering*, *194*(39), 4135-4195.

Kirchhoff, G. (1850). Über das gleichgewicht und die bewegung einer elastischen scheibe. *Journal für die reine und angewandte Mathematik*, *40*, 51-88.

Li, X., Zhang, J., & Zheng, Y. (2013). NURBS-based isogeometric analysis of beams and plates using high order shear deformation theory. *Mathematical Problems in Engineering*, *2013*, 9. http://dx.doi.org/10.1155/2013/159027

Loop, C., Schaefer, S., Ni, T., & Casta, I. (2009). Approximating subdivision surfaces with gregory patches for hardware tessellation. *ACM Transaction on Graphics*, *28*(5), 1-9. 10.1145/1618452.1618497

Melosh, R. J. (1963). Structural analysis of solids. *Journal of the Structural Division*, *89*(4), 205-248.

Mindlin, R. D. (1951). Influence of rotatory inertia and shear on flexural motions of isotropic, elastic plates. *J. appl. Mech.*, *18*, 31.

Mishra, B. P., & Barik, M. (2017). NURBS-augmented finite element method for static analysis of arbitrary plates. *Computers & Structures*, 1-13. https://doi.org/10.1016/j.compstruc.2017.10.011

Nanakorn, P., & Vu, L. N. (2006). A 2D field-consistent beam element for large displacement analysis using the total lagrangian formulation. *Finite Elements in Analysis and Design*, *42*(14), 1240-1247.

Neto, M. A., Amaro, A., Roseiro, L., Cirne, J., & Leal, R. (2015). *Engineering computation of structures: The finite element method*. Springer.

Oñate, E. (2013). *Structural analysis with the finite element method. Linear statics: Volume 2: Beams, plates and shells*. Springer Science & Business Media.

Peano, A. (1979). Conforming approximations for Kirchhoff plates and shells. *International Journal for Numerical Methods in Engineering*, *14*(9), 1273-1291.

Piegl, L., & Tiller, W. (1997). *The NURBS book*. New York: Springer.

Ranjan, R., & Reddy, J. N. (2018). Non uniform rational B spline (NURBS) based non-linear analysis of straight beams with mixed formulations. *Journal of Solid Mechanics*, *10*(1), 38-56.

Reali, A. (2006). An isogeometric analysis approach for the study of structural vibrations. *Journal of Earthquake Engineering*, *10*(spec01), 1-30.

Reissner, E. (1945). The effect of transverse shear deformation on the bending of elastic plates. *J. appl. Mech.*, A69-A77.

Rogers, D. (2001). An introduction to NURBS: With historical perspective. Morgan kaufmann. *San Francisco, CA*,

Shojaee, S., & Valizadeh, N. (2012). NURBS-based isogeometric analysis for thin plate problems. *Structural Engineering and Mechanics*, *41*(5), 617-632.

Szilard, R. (2004). *Theories and applications of plate analysis: Classical, numerical and engineering methods*. John Wiley & Sons.

Timoshenko, S. P., & Woinowsky-Krieger, S. (1959). *Theory of plates and shells*. McGraw-hill.

Vo, D. (2017). *A 2D field-consistent rational Bezier beam element for large displacement analysis*. Thammasat University.

Wanji, C., & Cheung, Y. (1997). Refined quadrilateral discrete Kirchhoff thin plate bending element. *International Journal for Numerical Methods in Engineering*, *40*(21), 3937-3953.

Zienkiewicz, O., & Cheung, Y. (1965). *Finite element procedures in the solution of plate and shell problems*. Chichester: John Wiley & Sons.

Zienkiewicz, O. C., & Cheung, Y. K. (1964). The finite element method for analysis of elastic isotropic and orthotropic slabs. *Proceedings of the Institution of Civil Engineers*, *28*(4), 471-488.

BIOGRAPHY

Name	Mr. Vithearin Chorn
Date of Birth	November 10, 1993
Education	2016: Bachelor of Engineering (Water Resources Engineering and Rural Infrastructure) Institute of Technology of Cambodia (ITC) 2019: Master of Science (Engineering and Technology) Sirindhorn International Institute of Technology Thammasat University